Vp-Vs Relations of Organic-rich Shales

A Thesis Presented to

the Faculty of the Department of Earth and Atmospheric Sciences

University of Houston

In Partial Fulfillment

of the Requirements for the Degree

Master of Science

By

Xuan Qin

August 2013

Vp-Vs Relations of Organic-rich Shales

_____

Xuan Qin

APPROVED:

_____

Dr. De-Hua Han, Chairman

_____

Dr. Hua-Wei Zhou

_____

Dr. Aibing Li

_____

Dr. Franklin Ruiz

Repsol Energy North America

_____

Dean, College of Natural Sciences and Mathematics

Acknowledgements

First, I would like to express my gratitude to my parents, who have been a pillar of strength throughout my life. Their financial and spiritual support has been the driving force in my graduate study. They set me a fine example of being righteous and exploring truths of our world.

I feel a deep sense of gratitude towards Dr. De-Hua Han for being an excellent supervisor. He trained me to shape good thinking habits with his brilliant knowledge of geosciences and physics, which made me feel strong, confident, and dedicated to work on my interests. I would also like to thank my committee member Dr. Franklin Ruiz for providing great suggestions on my research workflow and reviewing my work, as well as enthusiastic encouragements. Hereby I express sincere gratitude to my committee members Dr. Hua-Wei Zhou and Dr. Aibing Li, who encouraged me and taught me great skills of doing research and how to deal with academic problems with a clear and scientific mind.

I have been extremely fortunate to have the opportunity to share my time here at University of Houston, especially with colleagues in the Rock Physics Lab. I would like to thank Luanxiao Zhao for his excellent assistance on the rock physics models and his

inspiring discussions. Discussions with Dr. Quiliang Yao, Fuyong Yan, Min Sun, Hemin Yuan, Hui Li, Zhiwei Qian, Malleswar Yenugu, and Huizhu Zhao help me to make huge progress and to have a good understanding of rock physics. They have made my stay here in Houston a pleasurable time.

Xuan Qin

Houston, Texas

July, 2013

Vp-Vs Relations of Organic-rich Shales

An Abstract of a Thesis

Presented to

the Faculty of the Department of Earth and Atmospheric Sciences

University of Houston

In Partial Fulfillment

of the Requirements for the Degree

Master of Science

By

Xuan Qin

August 2013

Abstract

Organic-rich shales can serve as both source rocks and reservoir rocks. They are becoming increasingly important exploration and exploitation targets; however our knowledge of organic-rich shale properties is poor. Mudrock line (Castagna *et al.*, 1985) suggests that Vp/Vs ratios of shale are around 2, but Vp/Vs ratios of organic-rich shale vary from 1.5 to 1.7. What remains to be studied is what factors impact this difference. Understanding Vp-Vs relations for organic-rich source rock is vital for seismic characterization of shale reservoirs. This thesis explores several issues related to Vp-Vs relations of organic-rich shale, such as Vp/Vs ratio, P-wave and S-wave velocity anisotropies, and three Poisson's ratios in a TI medium.

Parameters that affect the Vp/Vs ratio in organic-rich shale are studied in two parts: mineralogy and organic matter. First, we studied Vp/Vs ratios, P-impedance, and velocity anisotropies in three types of organic-rich shales: silica-rich, clay-rich, and calcareous shales. Vp/Vs ratios change with mineral composition. A simple two-layer model built with the Backus average is used to explain why silica-rich shale has the highest shear anisotropy and calcareous shale has the highest P-wave anisotropy among the three types of organic-rich shale. Well logging data are utilized to separate the effects of quartz, clay, and calcite on Vp/Vs, P-impedance, and density. Second, total organic carbon (TOC) and maturation of organic matter significantly affect shale

properties, because of a large contrast between elastic properties of the organic and inorganic components. Basin and maturation models are built to simulate hydrocarbon generation during organic-rich shale evolution, which provides us the fundamentals for analyzing products and their concentrations in different maturation stages. The effect of organic matter with different maturity levels on immature, mature, and overmature shale properties are studied with rock physics models, which are based on effective medium theory. The immature and mature shale modeled results are plotted with the Bakken shale samples, which increase the credibility of the overmature model. The modeling results suggest that higher maturity level and TOC lead to lower Vp/Vs ratio and stronger anisotropy. When TOC is high, maturity level dominates; when TOC is low, TOC dominates.

Contents

List of Figures

List of Tables

Chapter 1 Introduction

1.1 Introduction to organic-rich shale

Shales are the most abundant sedimentary rocks in the earth's crust. Unconventional resources such as shale gas are becoming increasingly critical targets for exploration and exploitation, as the reservoir rocks are also the hydrocarbon source rocks.

In a conventional reservoir, shale is not considered as a reservoir rock. Rather, shale serves as a flow barrier, the seal rock, due to its low permeability which prevents hydrocarbons migration. Shale can, however, be a source rock which has the potential to generate hydrocarbons. However, as two technologies, horizontal wells and hydraulic fracturing, make huge progresses, the cost of exploiting hydrocarbons stored in shale has been significantly decreased. The recent significant growth of natural gas production has come from unconventional shale plays. Geophysical methods are considered to be critical in identifying shale reservoirs with the best potential production, which are often referred as sweet spots. Sweet spots in shale reservoirs may be defined on the basis of source rock richness, porosity, and natural fractures occurrence or brittleness, using geological data such as core, well logging, and seismic data.

Shale originates in the way presented in Figure 1.1.1. Initially, mud-sized (< 62.5 μm) particles are transported in suspension, which follows the Reuss (Mavko *et al.*, 2009)

bound and has a Poisson's ratio of 0.5. These particles settle out of suspension and begin to compact. New sediments deposited on the older sediment compact the underlying particles and cause the sheet-like particles to preferentially align, which contributes shale's intrinsic anisotropy. With the increase of burial depth and temperature, the dehydration of clay minerals occurs and shale's shear modulus increases. Compaction can dramatically reduce the porosity of shale; chemical cementation can also lower porosity and permeability (Dræge *et al.*, 2006). When the environment reaches the maturation conditions, hydrocarbons can be generated through a series of decomposition reactions (Luo and Vasseur, 1996; Carcione and Gangi, 2000).

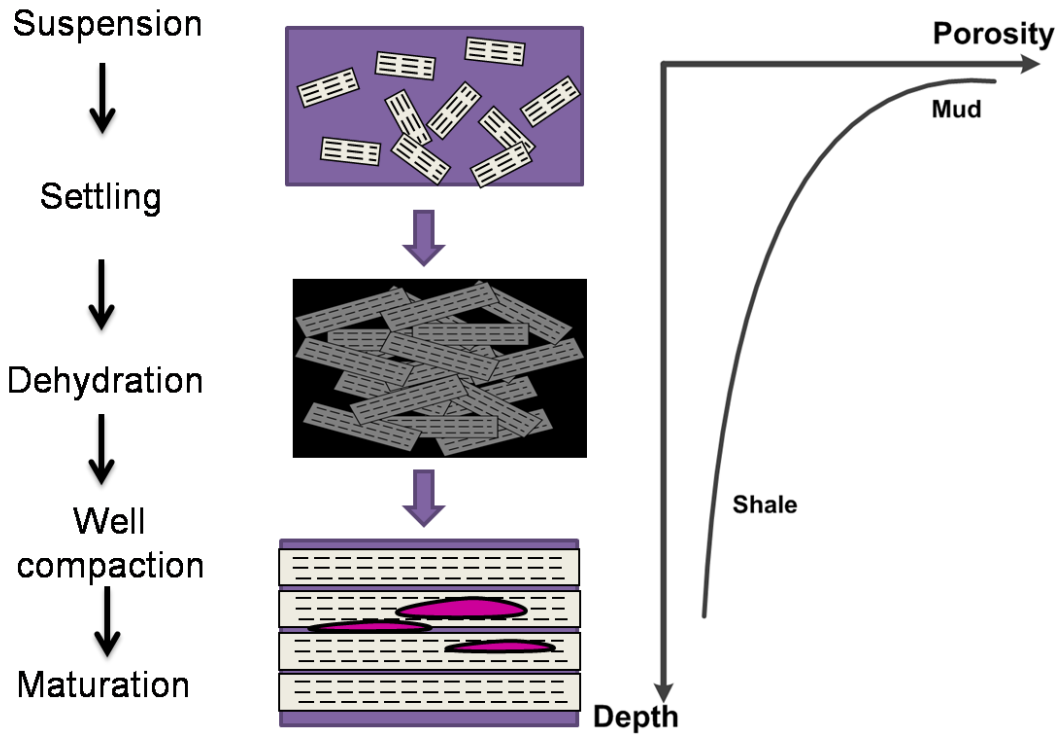

Figure 1.1.1 Schematic of organic-rich shale evolution.

To have a better understanding of elastic properties of unconventional source rocks, this thesis studies the effects of shale diagenesis, mineral composition, organic matter contents, and maturity levels on seismic properties of organic-rich shale.

1.2 Vp-Vs relations

P-wave and S-wave velocities are affected by compaction, cementation, porosity, water saturation, mineralogy, maturation, total organic carbon (TOC), stress, pore pressure, etc. For example, during shale formation, mud becomes compacted and cemented, which increases P-wave and S-wave velocity, but decreases the ratio of Vp/Vs. This is because compaction and cementation increase the resistance to shear deformation significantly, and S-wave velocity increases faster than does P-wave velocity. The ratio of P-wave to S-wave velocity, Vp/Vs, is sensitive to lithology and interstitial fluid, and will not change much with different P-wave or S-wave velocities; thus it can be used as a material indicator. The ratio is about 2 for many rocks, which is adopted in Shuey's AVO approximations (1985). This ratio is smaller for gas saturated rocks, and infinite for fluids.

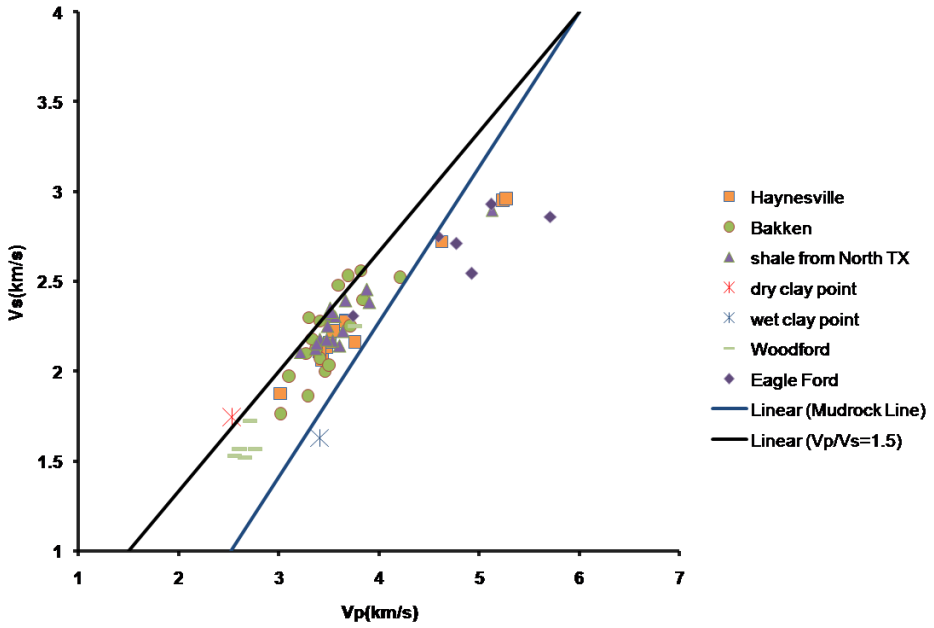

Figure 1.2.1 Normal-to-bedding P-wave (Vp0) and S-wave (Vsv) velocities of organic-rich shale samples from the Haynesville and Eagle Ford shales measured in the Rock Physics Lab at the University of Houston, the Bakken shale (Vernik and Liu, 1997), shale from north Texas (Karastathis, 2007), and the Woodford shale (Abousleiman et al., 2007). Some reference lines are plotted: black Vp/Vs equals to 1.5 and blue Castagna et al. (1985). Two reference points, red star and blue star, indicate dry clay point and wet clay point and are derived theoretically with Han's empirical equations (Han et al., 1986).

Figure 1.2.1 plots 59 organic-rich shale core samples normal-to-bedding P-wave and S-wave velocities. These samples consist of 12 Haynesville shale samples and 6 Eagle Ford shale samples measured by the Rock Physics Lab (RPL) at the University of Houston, 17 Bakken shale samples and 1 Woodford shale sample from Vernik and Liu (1997), 18 organic-rich shale samples from north Texas (Karastathis, 2007), and 5 Woodford shale samples from Abousleiman *et al.* (2007). The black solid line is constant Vp/Vs = 1.5; the blue solid line is the mudrock line (Castagna *et al.*, 1985), which describes Vp-Vs relation for uncompacted wet mudrock. Although most organic samples fall into the area between these two lines, the existing models relating Vp to Vs fail to apply to shales containing

even a few percent of organic material. Two reference points, a red star and a blue star, mark the dry clay point and the wet clay point respectively, and are derived theoretically from Han's empirical equations (Han *et al.*, 1986), assuming 0% porosity and 100% clay content. The dry clay point falls near the constant Vp/Vs of 1.5, indicating that when clay is dehydrated, clay minerals perform like quartz. The wet clay point falls near the mudrock line, whose P- and S-wave velocities behave like these in mudrock. In this thesis, factors such as mineral content, volume of organic matter, and maturity levels affecting organic-rich shales' Vp-Vs relations are studied and tried to be interpreted separately. Attributes like Vp/Vs, P-impedance, etc. are studied in samples with different mineral content and maturity levels.

1.3 Anisotropy

Anisotropy is defined as variation of a physical property depending on the direction in which it is measured. Shales are now universally recognized as being anisotropic (Johnston and Christensen, 1995; Jakobsen and Johansen, 2000; Sondergeld and Rai, 2011). Ignorance of shale anisotropy causes many an accuracy issue of seismic NMO correction, imaging, seismic Amplitude Variation with Offset (AVO), rock elastic stiffnesses, etc. Crystals exhibit intrinsic anisotropy and plate-like mineral grains and interstices tend to orient themselves parallel to sediment bedding, producing granular anisotropy. Besides organic matter alignments, micro-fractures parallel to bedding, and stress distribution also contribute to a certain degree of shale anisotropy.

Measurement of elastic anisotropies typically requires knowledge of the symmetry axis of shale. Shales are well-known for their layer-bedding structure, which can be considered to be transverse isotropic (TI) or polar anisotropic, with countless symmetry axes normal to the bedding. We expand two independent elastic constants in an isotropic medium, λ and μ, into five independent elastic stiffness constants c_{11}, c_{33} c_{44}, c_{66}, and c_{13} for a TI medium, which can be expressed in the form of an elastic stiffness tensor:

$$\begin{bmatrix} c_{11} & c_{12} & c_{13} & 0 & 0 & 0 \\ c_{12} & c_{11} & c_{13} & 0 & 0 & 0 \\ c_{13} & c_{13} & c_{33} & 0 & 0 & 0 \\ 0 & 0 & 0 & c_{44} & 0 & 0 \\ 0 & 0 & 0 & 0 & c_{44} & 0 \\ 0 & 0 & 0 & 0 & 0 & c_{66} \end{bmatrix}, \; c_{12} = c_{11} - 2c_{66}. \tag{1.3.1}$$

where c represents the stiffness constant. Energy considerations require that for elastic material with TI symmetry, the following conditions must hold (Mavko *et al.*, 2009):

$$c_{44} \geq 0, \; c_{11} > |c_{12}|, \; (c_{11} + c_{12})c_{33} > 2c_{13}^2. \tag{1.3.2}$$

These five independent elastic stiffnesses can be obtained from five velocity measurements (Figure 1.3.1): three P-wave velocities, $V_p(0°)$, $V_p(45°)$, and two S-wave velocities, $V_{SH}(90°)$, and $V_{SH}(0°) = V_{SV}(0°)$:

$$c_{11} = \rho V_p^2(90°), \tag{1.3.3}$$

$$c_{33} = \rho V_p^2(0°), \tag{1.3.3}$$

$$c_{44} = \rho V_{SH}^2(0°), \tag{1.3.4}$$

$$c_{66} = \rho V_{SH}^2(90°), \tag{1.3.5}$$

$$c_{13} = -c_{44} + \sqrt{4\rho^2 V_p^4(45°) - 2\rho V_p^2(45°)(c_{11} + c_{33} + 2c_{44}) + (c_{11} + c_{44})(c_{33} + c_{44})}\,, \quad (1.3.6)$$

where sub-indexes 1, 2, and 3 indicate axes X_1, X_2, and X_3. X_3 is the direction of symmetry; angles in the brackets in equations 1.3.3 to 1.3.6 represent angles between wave propagation and symmetry axes.

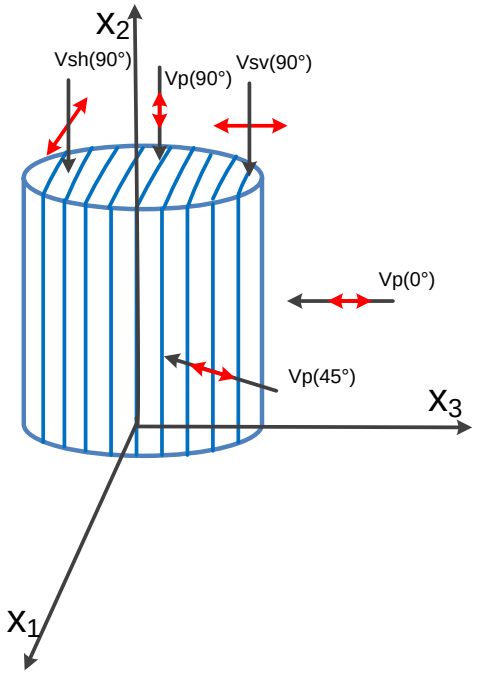

Figure 1.3.1 Schematic of shale sample and its transverse isotropic symmetry. X_3 is the symmetry axis; X_1 and X_2 are the axes parallel to the bedding. Angles in the brackets represent angles between wave propagation and symmetry axis. Black arrows indicate directions of three P-waves and two S-waves propagation. Red arrows indicate polarization direction of each wave.

To describe the weak elastic anisotropy in a TI medium, Thomsen (1986) parameterized the five elastic constants with following equations:

$$\alpha = \sqrt{\frac{c_{33}}{\rho}}\,, \quad (1.3.7)$$

$$\beta = \sqrt{\frac{c_{44}}{\rho}}, \tag{1.3.8}$$

$$\varepsilon = \frac{c_{11} - c_{33}}{2c_{33}}, \tag{1.3.9}$$

$$\gamma = \frac{c_{66} - c_{44}}{2c_{44}}, \tag{1.3.10}$$

$$\delta = \frac{(c_{13} + c_{44})^2 - (c_{33} - c_{44})^2}{2c_{33}(c_{33} - c_{44})}, \tag{1.3.11}$$

where α and β are the P-wave and S-wave velocities parallel to the symmetry, $V_p(0°)$ and $V_{SH}(0°)$. ε and γ are the P-wave and S-wave anisotropies, respectively. δ is a parameter that controls the velocity or slowness surface at polar angles to the principal direction.

1.4 Thesis overview

In this thesis, organic-rich shales are considered as TI mediums. The Vp/Vs ratios indicate the ratio of α/β, which corresponds to the sonic log velocities. To see the mineral effects on Vp/Vs ratios and velocity anisotropies of organic-rich shales, three types of organic-rich shales, (silica-rich, clay-rich, and calcareous shale,) are studied and analyzed in Chapter 2. Basin models reflect the evolution of organic-rich shale and provide us the basis to do rock physics modeling. The volume of organic matter and its maturity level also impact Vp-Vs relation as well as anisotropies of shale, which are studied in Chapter 3 by building rock physics models for three types of organic-rich shales classified by their maturity levels, i.e. immature, mature, and overmature. Chapter 4 is the summary of this thesis.

Chapter 2 Mineralogy effects on Vp-Vs relations of organic-rich shales

2.1 Mineralogy of organic-rich shales

The solid phase of organic-rich shale is generally composed of a variety of materials, such as clay minerals (illite, smectite, chlorite, kaolinite, etc.), non-clay silicate minerals (quartz, feldspar, plagioclase, etc.), carbonate minerals (calcite, ankerite, siderite, dolomite, etc.), and other minerals like pyrite, etc. When a wave propagates through the medium with a wavelength much larger than various granules or pores, its responses reflect the medium properties as a whole. The effective properties (velocities, anisotropies, and friability) of the shale matrix depend on comprehensive responses of these individual mineral's shape, orientation distribution, and volume fraction. Exploring rock matrix properties are meaningful in order to conduct further studies like fluid substitution (Gassmann, 1951; Biot, 1956) or solid substitution (Ciz and Shapiro, 2007).

North American unconventional plays develop fast and create enormous profit. However, different shale reservoirs vary considerably in their specific characteristics, such as heterogeneity, mineral composition, total organic carbon (TOC), organic matter maturation, etc. It is important to separate these factors' effects on organic-rich shales. The most common minerals in shales are clay, quartz, and carbonate; it is convenient to utilize a mineral triangle to estimate shale reservoir mineralogy. Figure 2.1.1 shows us

several shale reservoirs and their major mineral composition types shown in the ternary plot, where three vertices represent one of the three kinds of minerals reaching 100% volume fraction. Different colors represent mineral components in the Eagle Ford, Marcellus, Woodford, Horn River, Haynesville, and Wealden shales. For example, the Eagle Ford reservoir rock (blue color) is characterized as calcareous shale, which underlies the Austin Chalk. Other unconventional plays, such as the Marcellus (red color), Haynesville (yellow color), etc., also contain large amount of calcareous shales. The Woodford shale (black color) is generally composed of quartz, illite, chlorite, dolomite, and pyrite, but its quartz volume is dominant (Abousleiman *et al.*, 2007); we can classify it as a "silica-rich" shale. It is similar to the Horn River shale (green color). "Clay-rich" shale plays are less common than the other two kinds of reservoir rock.

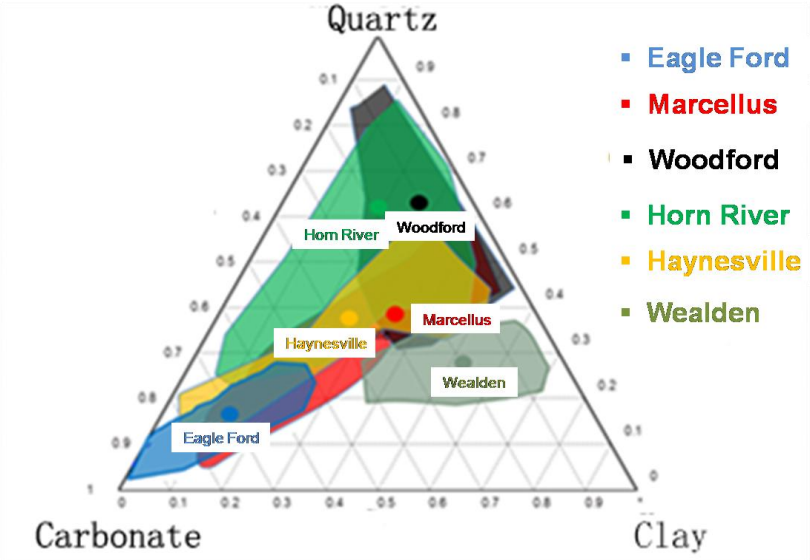

Figure 2.1.1 Shale plays in the U.S. and their classifications based on mineral triangle. Each vertice represents that one kind of mineral reaches 100% in rock matrix. Blue, red, black, green, yellow, and cyan areas represent mineral components in the Eagle Ford, Marcellus, Woodford, Horn River, Haynesville, and Wealden shales (modified from Passey et al., 2011).

2.2 Mineralogy effects on Vp-Vs relations of organic-rich shales

This chapter discusses the effects of minerals on three types of organic-rich shales: calcareous shales, silica-rich shales, and clay-rich shales. Zhu *et al.* (2011) used rock physics model-based templates to describe relationships between the Vp/Vs ratio and P-impedance for silica-rich and clay-rich rocks. We collected North American unconventional shale reservoir core data from several sources (Vernik and Liu, 1997; Abousleiman *et al.*, 2007; Karastathis, 2007); and core data measured in the Rock Physics Lab at the University of Houston, included in Table 2.2.1. Mineralogical effects on Vp-Vs relations of organic-rich shales are studied based on their component mineralogy. Shale sample data have been checked with proper rock physics constraints. For example, Thomsen anisotropic parameters ε and γ should be positive (Thomsen, 1986). Therefore, we discard data outside of these constraints.

Table 2.2.1 Organic-rich shale sample core data used in this thesis.

Data Source	Unconventional Play	Number of Samples	Mineralogy Types
Abousleiman *et al.* (2007)	Woodford shale	5	Silica-rich
Vernik and Liu (1997)	Woodford shale	1	Silica-rich
Karastathis (2007)	Shale from north Texas	18	Clay-rich
RPL	Haynesville	13	Calcareous
RPL	Eagle Ford shale	7	Calcareous

Figures 2.2.1 plots Vp/Vs (normal-to-bedding velocities) and P-wave impedance data for organic-rich shales. Data shown with the blue dashed points in these figures are the silica-rich type of organic-rich shales, from the Woodford shale (Vernik and Liu, 1997;

Abousleiman *et al.*, 2007). Their average mineral compositions, by volume, are 41.1% silica, 6.5% carbonates, 29.9% clay, and 14.7% kerogen, with some other minor (< 7.8%) minerals such as pyrite. Data shown with the yellow circles (Figure 2.2.1) are the results from silica-rich shales from north Texas (Karastathis, 2007), with an average weighted mineral composition of 35% clay, 31% quartz, and 17% carbonate and some other minerals. The green squares (Figure 2.2.1) indicate calcareous shale samples from the Haynesville and Eagle Ford formations measured in the Rock Physics Lab at the University of Houston.

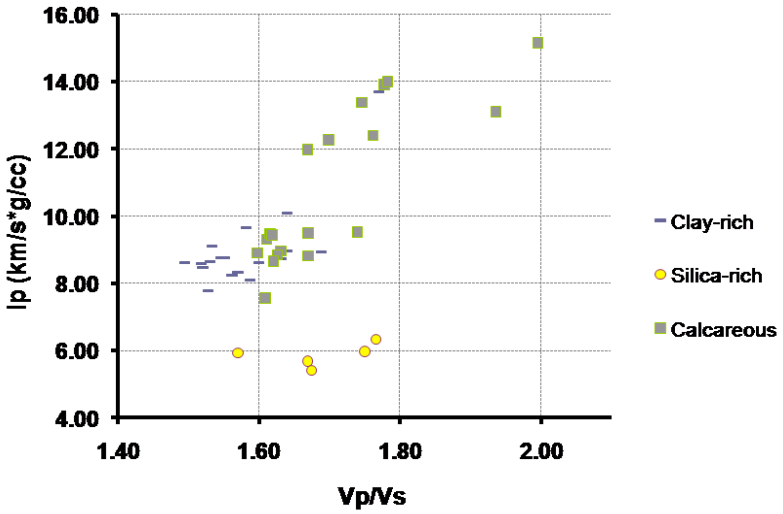

Figure 2.2.1 P-impedane vs. Vp/Vs for three types of organic-rich shales: clay-rich shales from north Texas (Karastathis, 2007), silica-rich shales from the Woodford Shale (Abousleiman et al., 2007), calcareous shales from the Haynesville and Eagle Ford shales measured in the Rock Physics Lab at the University of Houston and the Woodford Shale (Vernik and Liu, 1997).

The Vp/Vs ratios versus P-impedance values for the three types of organic-rich shales are plotted on Figure 2.2.1. For clay-rich shale samples, their Vp/Vs ratios range from 1.5 to 1.78 and the Vp/Vs ratios for silica-rich shales range from 1.55 to 1.76. Calcareous shales

have Vp/Vs ratios ranging from 1.6 to 1.99. The Vp/Vs ratios for calcareous shales are mostly higher than the other two types. Lower values of Vp/Vs in silica-rich shales are mainly due to the large amount of quartz. The shear modulus of quartz is 44 GPa and is higher than its bulk modulus at 37 GPa. Such a low K/μ ratio is responsible for the low Vp/Vs ratio of pure sandstone and silica-rich shales with large amounts of quartz:

$$\left(\frac{V_p}{V_s}\right)^2 = \frac{K}{\mu} + \frac{4}{3}. \tag{2.2.1}$$

Silica-rich shales from the Woodford formation contain higher porosities (17.2% on average) than clay-rich shales from north Texas (6.2% on average). Increasing porosity decreases Vp and Vs, but Vs decreases more rapidly, which can be derived from Han's empirical relations (Han *et al.*, 1986). Low porosities also account for the low P-impedance of these silica-rich shale samples. Although clay mineral content can raise Vp/Vs, we can theoretically derive the "dry clay point" with a Vp/Vs ratio equal to 1.46 and the "wet clay point" with a Vp/Vs ratio of 2.09 with Han's empirical equations (Han *et al.*, 1986), which describe relationships between velocities and porosity as well as clay content for shaly sand. No shale is dry under atmospheric conditions, and the properties of clay closely depend on its water content. Free water is present in the mineral pores, and adsorbed water is located at the surface of clay particles. Bound water exists between the clay platelets, which is responsible for the low shear modulus of clay minerals. Crystalline water forms part of the crystalline structure of minerals, which requires a temperature above 500 ℃ to be removed (Sarout and Guéguen, 2008). If the pore fluid salinity is high, clay will lose water to reach salinity equilibrium and become more rigid; if the salinity is low, clay will suck water, making it swelling and less rigid. Since clay

properties vary siginificantly with its water content, its Vp/Vs ratio has a large range. This can serve to explain why the Vp/Vs ratios of clay-rich shales can be lower than that of silica-rich shales. All in all, it is vital to know the clay mineral properties when measuring in a laboratory or when well logging in the field. Both the Vp/Vs ratio and P-impedance of calcareous shales are overall higher than those of clay-rich and silica-rich shales. Calcite minerals have a density of 2.71 g/cc, a bulk modulus of 77 GPa, and shear modulus of 32 GPa (Mavko *et al.*, 2009). Thus, increasing the carbonate content can increasing the Vp/Vs ratio and P-impedance. However, the three calcareous shales have Vp/Vs ratios close to 1.6, and this is maybe because calcite forms the cement material. When the in-situ temperature is high, organic matter can produce hydrocarbons. If the shale's permeability is too low to allow byproducts, such as CO_2 and water, to run out in time, it will finally lead to the precipitation of calcite. Cementation decreases the rock Vp/Vs ratio as cement materials between mineral grains, which help rocks to resist shear deformation.

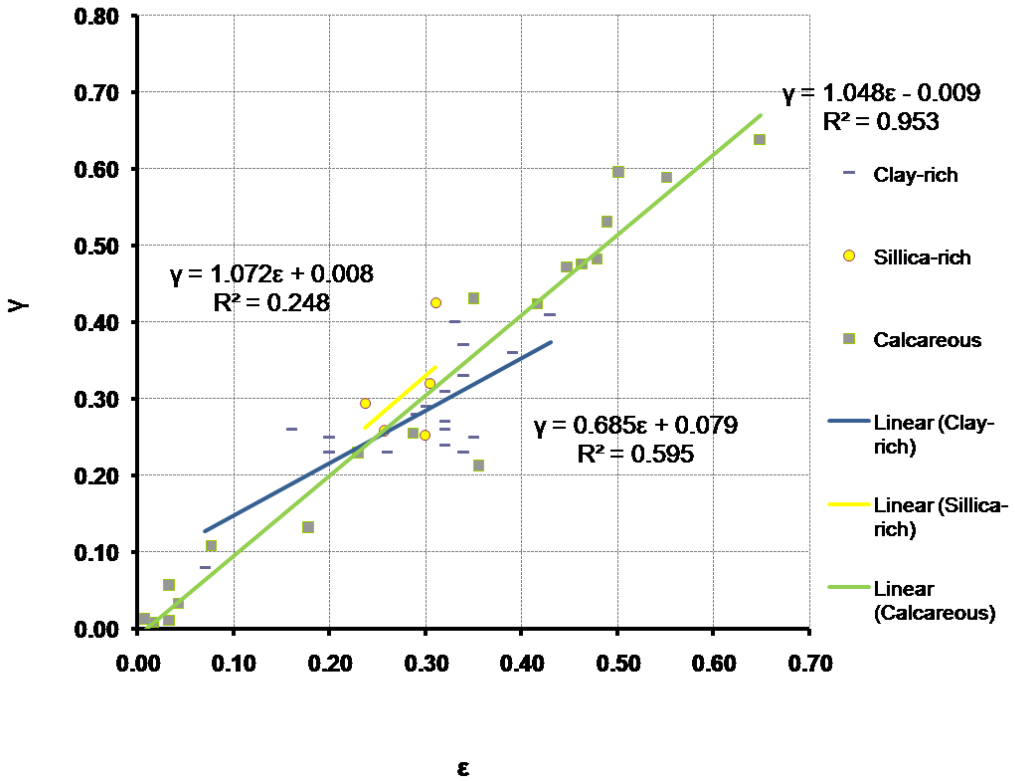

Figure 2.2.2 P-wave anisotropy ε vs. S-wave anisotropy γ for clay-rich shales from north Texas (Karastathis, 2007), sillica-rich shales from the Woodford Shale (Abousleiman et al., 2007) and calcareous shales from the Haynesville and Eagle Ford shales measured in the Rock Physics Lab at the University of Houston and the Woodford shale (Vernik and Liu, 1997) .

Figure 2.2.2 plots P-wave anisotropy (ε) and S-wave anisotropy (γ) for clay-rich shales (blue dashed points), sillica-rich shales (yellow circles), and calcareous shales (green squares). As a whole, these data points show an approximately linear trend with a slope of 1 to describe P- and S-wave anisotropies. Their individual linear regression equations are shown in the figure. Specifically, for calcareous shales, the linear approximation has the highest model resolution matix of R^2 = 0.953, thereby ε and γ are almost equal. Among sillica-rich shale samples, γ is normally larger than ε with the poorest model

resolution. Among clay-rich shale samples, γ is normally less than ε with an intermediate model resolution. All these trend features of different mineral contents can provide us with thoughts on organic-rich shales mineralogy studies.

The Backus average (Backus, 1962) is applied to interpret the relationship between the P-wave and S-wave anisotropies for these three types of shales. Rock is assumed to be a two-layer medium composed of either clay and quartz, which is used to simulate silica-rich shale, or clay and calcite, which is used to simulate calcareous shale (Figure 2.2.3). The Backus average gives a transversely isotropic effective medium when wave propagates in the multilayer medium with a wavelength much larger (at least 10 times) than the thickness of individual layer. In a TI medium, the effective elastic stiffness constants are given by:

$$\overline{c_{11}} = \left\langle c_{11} - c_{13}^2 c_{33}^{-1} \right\rangle + \left\langle c_{33}^{-1} \right\rangle^{-1} \left\langle c_{33}^{-1} c_{13} \right\rangle^2, \tag{2.2.2}$$

$$\overline{c_{33}} = \left\langle c_{33}^{-1} \right\rangle^{-1}, \tag{2.2.3}$$

$$\overline{c_{13}} = \left\langle c_{33}^{-1} \right\rangle^{-1} \left\langle c_{33}^{-1} c_{13} \right\rangle, \tag{2.2.4}$$

$$\overline{c_{44}} = \left\langle c_{44}^{-1} \right\rangle^{-1}, \tag{2.2.5}$$

$$\overline{c_{66}} = \left\langle c_{66} \right\rangle, \tag{2.2.6}$$

where c_{ij} are the stiffnesses corresponding to the single constituents, in this case of clay and quartz, or clay and calcite, and $\langle \cdot \rangle$ indicates weighted average. Clay mineral is treated as a TI medium with elastic stiffnesses: c_{11} = 44.9 GPa, c_{33} = 24.2 GPa, c_{44} = 3.7 GPa, c_{66} = 11.6 GPa, and c_{13} = 18.1 GPa (Sayers, 2013). The bulk and shear moduli of

quartz are 37 GPa and 44 GPa, respectively; bulk and shear moduli of calcite are 77 GPa and 32 GPa, respectively. These mineral properties are listed in Table 2.2.2.

Table 2.2.2 Mineral elastic stiffnesses used in the two-layer model.

Mineral	c11(GPa)	c33(GPa)	c44(GPa)	c66(GPa)	c13(GPa)	ε	γ	δ
Clay	44.9	24.2	3.7	11.6	18.1	0.43	1.07	0.06
Quartz	95.7	95.7	44	44	7.7	0	0	0
Calcite	119.5	119.5	32	32	55.5	0	0	0

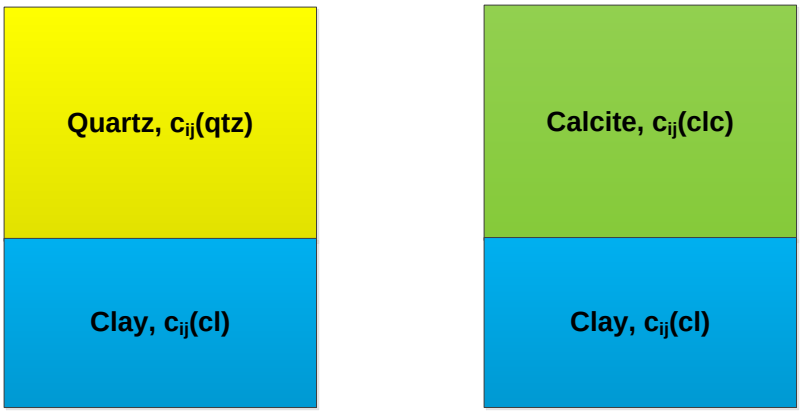

Figure 2.2.3 Left: two-layer model of silica-rich shale. Right: two-layer model of calcareous shale.

In order to investigate the influence of different mineral content on rock effective properties, we set up simple two-layer models as follows: quartz volume fraction is over 50% in silica-rich shale model (Figure 2.2.3 (left)) and calcite volume fraction is over 50% in calcareous shale model (Figure 2.2.3 (right)). Then we can calculate rock

effective properties with constituents (quartz and calcite) ranging in volume from 50% to 100%.

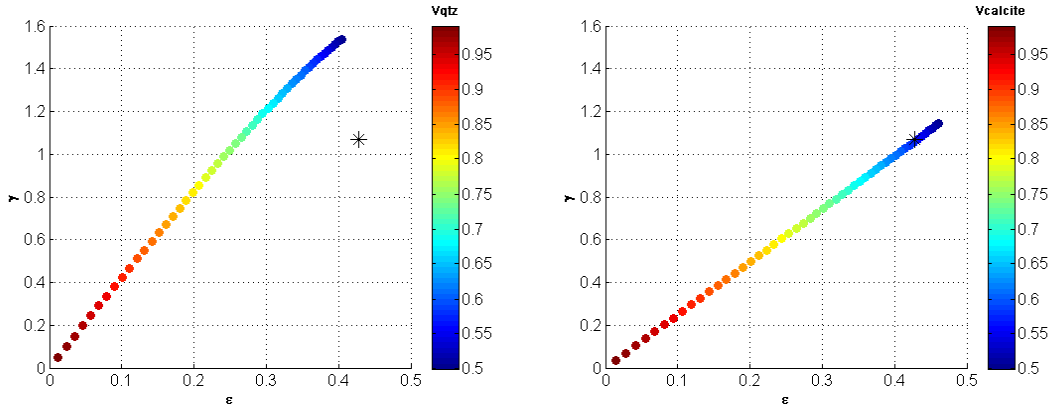

Figure 2.2.4 *Two-layer Backus modeled silica-rich shales (quartz volume fraction larger than 50%) and calcareous shales (calcite volume fraction larger than 50%) P-wave and S-wave anisotropies. Black stars indicate pure clay P-wave and S-wave anisotropies. Quartz and calcite volume fractions are color-coded, respectively.*

Figure 2.2.4 demonstrates that for silica-rich shale model, γ/ε ratio is close to 4; with an increase of quartz volume ($V_{qtz} > 50$), γ/ε ratio remains approximately constant and values of γ and ε gradually decrease to zero. This can explain why γ is larger than ε in the trend line of silica-rich shales in Figure 2.2.4. For calcareous shales, the γ/ε ratio is close to 2.5; similarly, with an increase of calcite content, γ/ε ratio remains approximately constant and values of γ and ε gradually decrease to zero. Although γ/ε does not equal to 1 in Figure 2.2.2, we can suggest that silica-rich shales have larger γ/ε than calcareous shales. The black star "*" represents P- and S-wave velocity anisotropies of pure clay mineral. Adding quartz content into pure clay can cause S-wave anisotropy to increase but P-wave anisotropy to decrease. Adding calcite to pure clay initially increases both S-wave anisotropy and P-wave anisotropy, but soon decreases both of them at a roughly

constant γ/ε ratio. Because in the Backus average, Voigt average is used to approximate $\overline{c_{66}}$, which is the maximum value. Reuss average is used to approximate $\overline{c_{33}}$ and $\overline{c_{44}}$, which are the minimum values; therefore, this method overestimates ε and γ. Comparing the overestimation of γ/ε using the Backus average with Figure 2.2.2, for the parameters c_{11} and c_{33}, the difference between calcite and clay is larger than that between quartz and clay, and thus, we can deduce that ε increases more rapidly due to calcite. For the parameters c_{44} and c_{66}, the difference between quartz and clay is larger than that of calcite and clay, and consequently, we can deduce that γ increases more rapidly due to quartz. In a word, γ/ε ratios seem to be constant for silica-rich and calcareous shales, which may be used as a mineral composites indicator.

Thomsen anisotropic parmeter δ, one of the most important parameters for exploration geophysicists to determine the NMO velocity in a TI medium, is the difference between the P-wave and SV-wave anisotropies of the medium. The difference between ε and δ, $\eta' \equiv \varepsilon - \delta$, is termed as "anellipticity" to describe the deviation between P-wave front and elliptical wave front (Thomsen, 2002). If η' = 0, P-wave front reduce to an ellipse with ε = δ. In Figure 2.2.5, there can be a linear trend to describe ε and δ behavior in calcareous shales:

$$\varepsilon = 1.234\delta - 0.1,\ R^2 = 0.661. \qquad (2.2.7)$$

It is unreliable to derive a linear relation for silica-rich shales due to a paucity of sample data. For clay-rich shales, the data points in ε-δ plane are scattered, δ varies from negative values to positive values, and sometimes can be quite high. The linear trend

between ε and δ suggests that we can refer to such a correlation when studying calcareous shale reservoir.

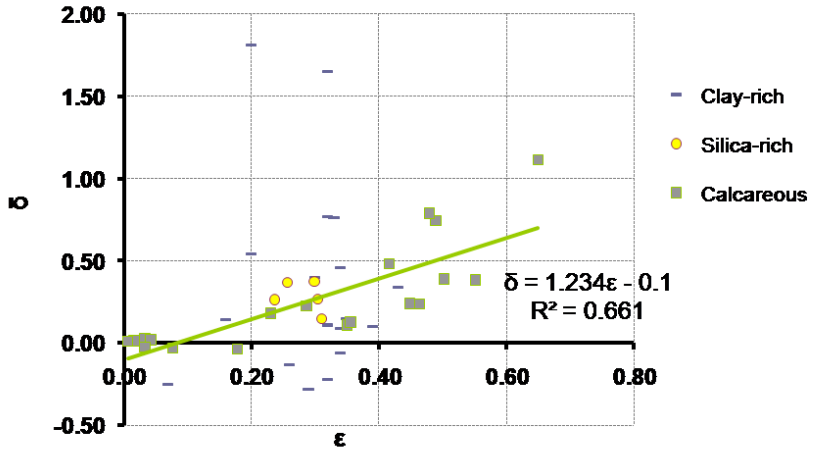

Figure 2.2.5 Thomsen anisotropic paramters ε vs. δ for clay-rich, sillica-rich, and calcareous shales.

For a TI medium, we can use three Poisson's (Mavko *et al.*, 2009) to study anisotropic material. Let's consider a TI material with uniaxial stress, applied along the symmetry (x_3-) axis. A Poisson's ratio can be defined as:

$$\nu_{31} = -\frac{\varepsilon_{11}}{\varepsilon_{33}} = \frac{C_{13}}{C_{11} + C_{12}}, \tag{2.2.8}$$

where ε_{11} is the strain of bedding plane due to stress along the symmetry, ε_{33} is the strain along the symmetry and C_{ij} are the elastic stiffnesses. If the uniaxial stress is rotated normal to the symmetry axis, another two Poisson's ratios can be defined as:

$$\nu_{13} = -\frac{\varepsilon_{33}}{\varepsilon_{11}} = \frac{C_{13}(C_{11} - C_{12})}{C_{11}C_{33} - C_{13}^2}, \tag{2.2.9}$$

$$\nu_{12} = -\frac{\varepsilon_{22}}{\varepsilon_{11}} = \frac{C_{12}C_{33} - C_{13}^2}{C_{11}C_{33} - C_{13}^2}, \tag{2.2.10}$$

where ν_{13} is the negative ratio of strain parallel to the symmetry to the strain in the bedding plane due to the uniaxial parallel to bedding stress, and ν_{12} is the negative ratio of strain parallel to the bedding and normal to the stress to the strain in the bedding plane and along the stress. Figure 2.2.6 demonstrates scenarios of ν_{31} (left) and ν_{13} (right).

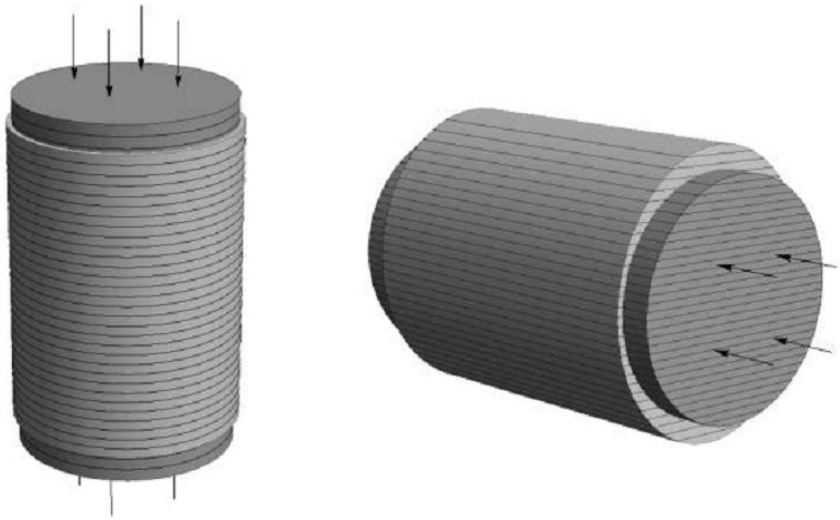

Figure 2.2.6 Schematic deformation of vertical plug (left) and horizontal plug (right) of transverse isotropic rocks under compression along the symmetry and bedding, respectively. Dark grey represents before compaction; light grey represents after compaction (Yan and Han, 2013).

Their bounds are defined as

$$|\nu_{31}| \le \left(\frac{E_{33}}{E_{11}}\right)^{1/2}, \; |\nu_{13}| \le \left(\frac{E_{11}}{E_{33}}\right)^{1/2}, \; |\nu_{12}| \le 1, \tag{2.2.11}$$

where E_{11} and E_{33} are Young's Moduli along the bedding and parallel to symmetry in the TI medium. From equation 2.2.8, since C_{11}, C_{12}, and C_{13} are positive, ν_{31} is positive. For

the TI medium, the Young's modulus in horizontal direction should always be larger than that in vertical direction (E11 > E33), it is also satisfied that

$$\nu_{13}E_{33} = \nu_{31}\mathrm{E}_{11}, \tag{2.2.12}$$

therefore,

$$\nu_{13} > \nu_{31} > 0. \tag{2.2.13}$$

These constraints can be modified as:

$$0 < \nu_{31} \le \left(\frac{E_{33}}{E_{11}}\right)^{1/2}, \; 0 < \nu_{13} \le \left(\frac{E_{11}}{E_{33}}\right)^{1/2}, \; |\nu_{12}| \le 1, \tag{2.2.14}$$

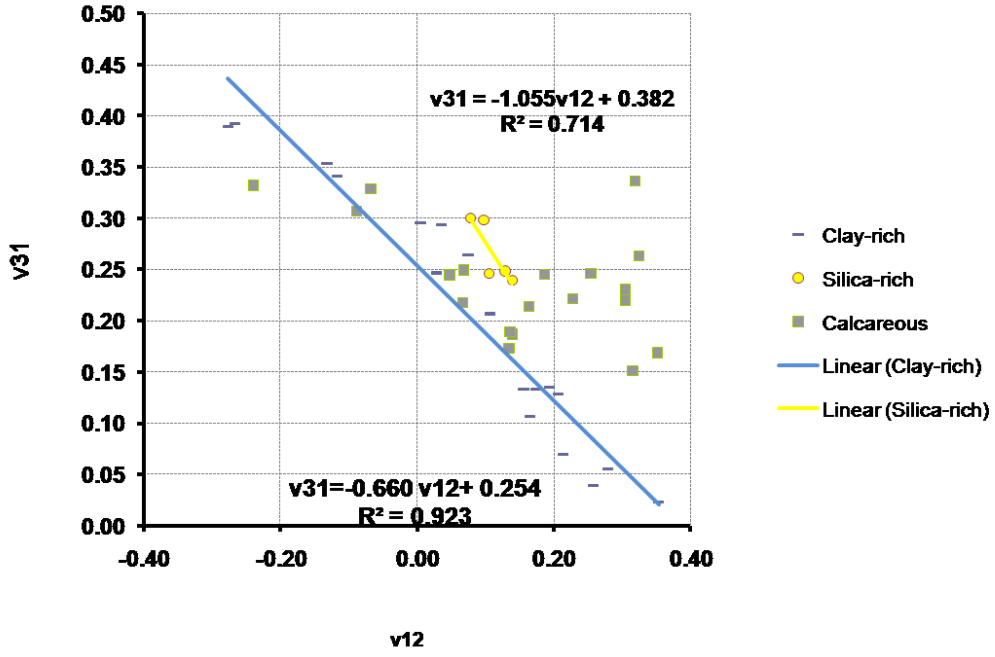

Figure 2.2.7 Poisson's ratios ν_{12} vs. ν_{31} for clay-rich, sillica-rich, and calcareous shales. A linear trend can be obtained for clay-rich and silica-rich shales.

Figure 2.2.7 displays the relation between ν_{12} and ν_{31} for clay-rich, silica-rich, and calcareous shales. All of ν_{31} values of these samples are positive, but ν_{12} of clay-rich and calcareous shales can be negative. ν_{31} decreases with increasing ν_{12} as a whole. For samples with negative ν_{12}, their δ values are all larger than 0.5. We can use a good linear approximation to describe the relationship between ν_{12} and ν_{31} for clay-rich shale samples from north Texas:

$$\nu_{31} = -0.660\nu_{12} + 0.254,\ R^2 = 0.923. \tag{2.2.15}$$

Silica-rich shales seem to be able to use a linear approximation to describe the relationship between ν_{12} and ν_{31}:

$$\nu_{31} = -1.055\nu_{12} + 0.382,\ R^2 = 0.714. \tag{2.2.16}$$

Poisson's ratios in the TI medium can provide us strategies when studying rock geomechanic properties and devising hydraulic fracturing. The relationships between ν_{12} and ν_{31} in silica-rich and clay-rich shales provide us thoughts on lithology analysis and rock mechanics study.

2.3 Example from the Barnett shale

Core sample analysis provides us organic-rich shale velocities and velocity anisotropies information. However, we sometimes miss reports of sample compositions. Not only does the well logging suite provide us information of formation sonic travel time, gamma ray, resistivity, neutron porosity, density, etc., but its comprehensive interpretation also

provides us information of mineral types and fractions. So in this section, we study mineral effects on the organic-rich shales with well logging data.

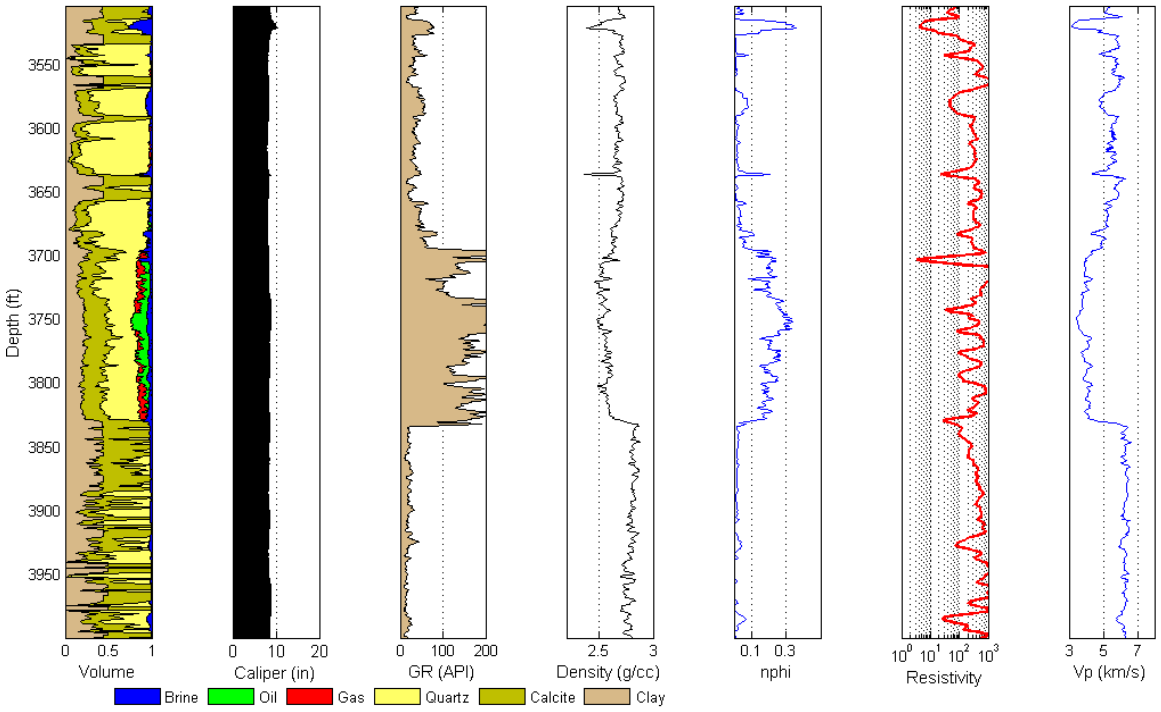

Figure 2.3.1 Well logging curves of the Barnett Shale. From left to right: volume fraction of each component, caliper log (inch), gamma ray log (API), density log(g/cc), neutron porosity, resistivity and P-wave velocity.

Figure 2.3.1 shows us logging data from the Barnett shale, including mineral and pore fluid volume fraction, caliper log, gamma ray, density, neutron porosity, resistivity, and P-wave velocity. The depth of target zone is from 1128 m to 1167 m. In this zone, mineral compositions are mainly assumed to consist of quartz, clay, and calcite. Other minerals such as pyrite, siderite, ankerite, etc. are neglected since they are minor (< 10%) in the shale reservoir. In the target layers, gamma ray (GR) is abnormally high, which count both clay and total organic carbon (TOC) (Passey, 1990). Its density is lower than

upper and lower layers, due to larger porosities and lighter pore fluid, gas and oil. In the hydrocarbon zone, due to gas effect, neutron porosity increases, resistivity increases and P-wave velocity decreases.

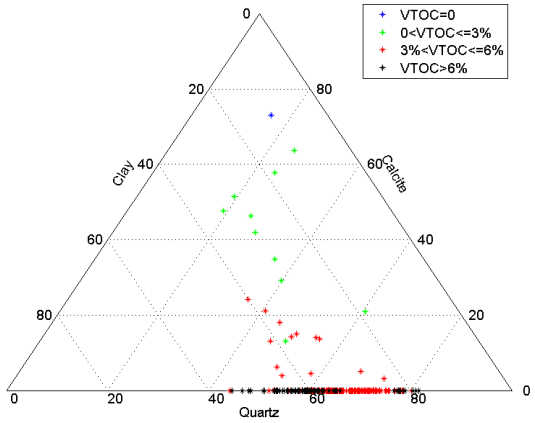

Figure 2.3.2 Ternary plot for mineral composition of the Barnett shale. TOC is color-coded with different values. Upper vertice is the point when calcite content reaches 100%, lower left vertice is the point when clay content reaches 100%, and lower right vertice represent the point when quartz volume fraction reaches 100%.Blue stars represent Volume of Total Organic Carbon (VTOC) equals to 0, green stars represent VTOC less than 3%, red stars represent VTOC between 3-6%, and black stars represent VTOC higher than 6% for that depth.

The Barnett shale is usually considered as silica-rich shale. Figure 2.3.2 shows us the ternary mineral plots for the target zone from 1128 m to 1167 m, with three vertices as 100% quartz, clay and calcite. Higher TOC (red and black star) mainly aggregates at shales, which consist of higher amount of quartz (40-80%) and higher amount of clay (20-60%).

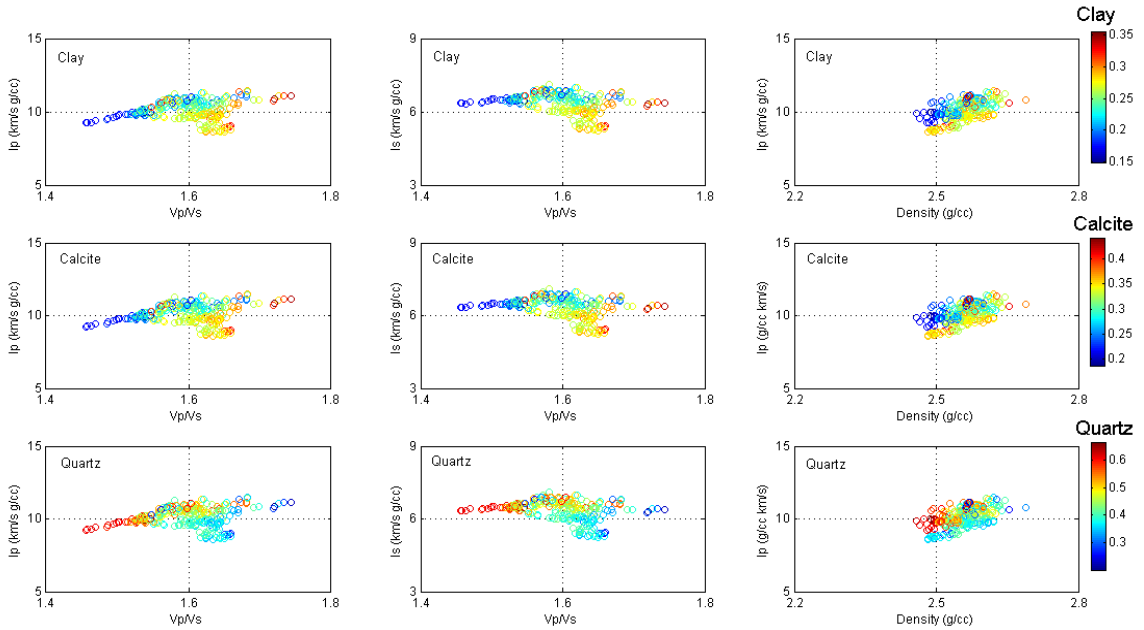

Figure 2.3.3 Crossplots of P-impedance vs. Vp/Vs, S-impedance vs. Vp/Vs, and P-impedance vs. Density color-coded with clay, calcite and quartz volume fractions, respectively. For the same row, all of crossplots are color-coded with the same mineral volumes. For the same column, all of crossplots' axes share the same attributes (P-impedance, S-impedance, Vp/Vs or Density), and scales.

Due to similar pore fluids compositions and porosities, these in-situ measurements can show us each kind of mineral composition effects if we can plot them properly. We use crossplots (Figure 2.3.3) of P-impedance vs. Vp/Vs, S-impedance vs. Vp/Vs, and P-impedance vs. density to separate effects of clay, calcite, and quartz minerals in organic-rich shale. Minerals are color-coded with their volume fractions; cold color represents low concentrations and warm color represents high concentrations, respectively. Quartz volume fraction varies from 20% to 65%, clay volume fraction ranging from 15% to 35%, and calcite volume fraction ranging from 20% to 45%. For silica-rich shales, where quartz dominates rock matrix composition, (i.e. over 50%), Vp/Vs ratios can be as low as 1.5 to 1.6. This agrees with the rock physics models by Zhu *et al.* (2011), where silica-

rich shales with the highest amount of quartz content have the lowest Vp/Vs ratios. With the lowest volume fraction of quartz (20%) and the highest amount of clay and calcite, Vp/Vs ratios can be as high as 1.75. Both clay and calcite play roles of increasing Vp/Vs ratios, because mineral K/μ ratios of clay and calcite are larger than quartz's.

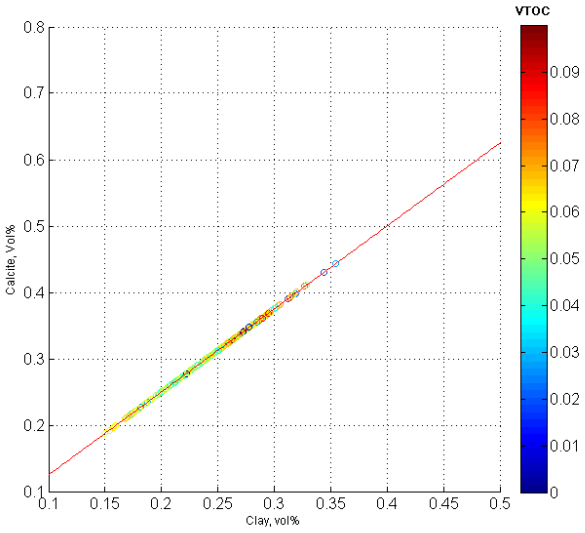

Figure 2.3.4 Crossplot of clay volume fraction vs. calcite volume fraction, color-coded with volume of total organic carbon. Clay content shows a good correlation with calcite content in this silica-rich shale reservoir. This mineralogy interpretation work was done by Marathon Oil Company and a linear correlation was assumed.

Figure 2.3.4 shows us that in this silica-rich reservoir, clay content correlates with calcite content closely:

$$V_{clc} = 1.25V_{cl} - 1.4\times10^{-6},\ R^2 = 1. \qquad (2.3.1)$$

In Figure 2.3.3, where clay and calcite are most abundant, 40% and 30%, respectively, silica-rich shales can have a higher Vp/Vs ratio larger than 1.65, but its P-impedance has either the lowest value of 8 km/s*g/cc due to clay, or the highest value of 12 km/s*g/cc

due to calcite. At the same density values, increasing quartz content causes an increase of P-impedance for the Barnett shales.

Chapter 3 Organic matter effects on Vp-Vs relations of organic-rich shales

3.1 Maturation of organic-rich shales

Organic matter can be frequently found in source rocks and unconventional reservoir rocks. Figure 3.1.1, a scanning electron microscope (SEM) image of the Barnett shale sample, shows us that black organic carbon, which is indicated with "C," can be coated with argillaceous minerals. Organic matter in the form of amorphous kerogen has the potential to generate hydrocarbon. The process of the biological, physical, and chemical decomposition of kerogen into hydrocarbons is called as maturation.

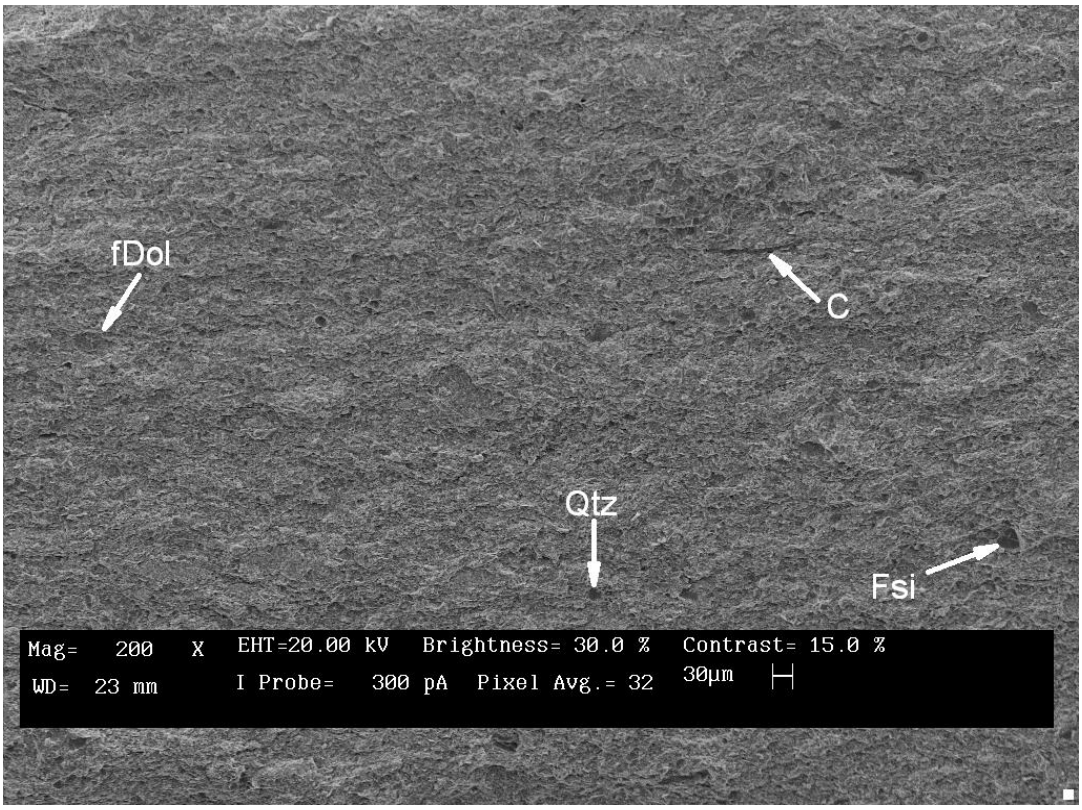

Figure 3.1.1 SEM image of the Barnett shale sample at 1129.4 m. It shows mixed siliceous/argillaceous mudstone viewed at low magnification to illustrate the general texture. Stringers of black organic carbon (C) and compressed lenses of carbonates such as ferroan dolomite (fDol) lie along parallel laminations. Quartz (Qtz) is the dominant detrital grain, while the fossils include silica-replaced shell fragments (Fsi). (Courtesy of Marathon Oil Company)

Maturation begins within organic-rich sedimentary layers being deposited. There are two possible means of hydrocarbon generation (Seewald, 2003). First, kerogen can form a macromolecular bitumen phase, followed by the decomposition of bitumen to form liquid oil and gas. Second, oil and gas may be produced directly from kerogen without a bitumen intermediary. Initially, a series of low-temperature (<50 ℃) reactions occurs, which involves anaerobic bacteria reducing the oxygen, nitrogen, and sulphur in the kerogen, leading to an increased concentration of hydrocarbon compounds. This stage continues until the temperature of the source rock reaches about 50 ℃. Thereafter, the

effect of elevated temperature becomes much more pronounced as the reaction proceeds. Organic-rich shales' properties, such as elasticity, density, and porosity, change during maturation. Kerogen can decompose to produce oil and gas, create pore space within the organic matter, and leave the final product of graphite. Bedding-aligned micro-cracks can be found during maturation. When the temperature of buried shale increases, organic matter decomposes into oil and gas, leaving its original space with kerogen-related pores. Abnormal high pore pressure due to hydrocarbon generation frequently accompanies gas shale reservoirs. If the generated oil and gas are pumped out due to high pore pressure, the pore spaces can close. Afterwards, more hydrocarbons are generated, leading to overpressure and "pump out." When the active organic matter has almost fully decomposed, the space left can be closed by the overburden pressure or cemented with calcite, which is formed during reactions of other minerals with CO_2 generated during maturation.

Since temperature increases with depth in the Earth, heating is naturally achieved by burial of the source rock. The actual temperature reached at a given depth depends on the rate of the temperature increase with depth, the geothermal gradient. Figure 3.1.2 (left) demonstrates four types of kerogen evolving to maturation with the maturation indicators of vitrinite reflectance (%Ro) or the atomic ratios of hydrogen to carbon (H/C) and oxygen to carbon (O/C). The H/C indicator mainly shows the potential of hydrocarbon generation (kerogen type); the O/C indicator suggests the progress of the maturation reaction. Figure 3.1.2 (right) shows the relative proportions of crude oil and gas formed from type II kerogen buried in an area with a geothermal gradient of about 35 ℃/km.

Significant amounts of hydrocarbons begin to form at temperatures over 50 ℃, and the largest quantity of petroleum is formed as the kerogen is heated to temperatures between 60 and 150 ℃. At higher temperatures, oil becomes thermally unstable and breaks down or "cracks" to become natural gas. Even after maturation, some of the inactive kerogen remains unaltered as a carbon-rich residue.

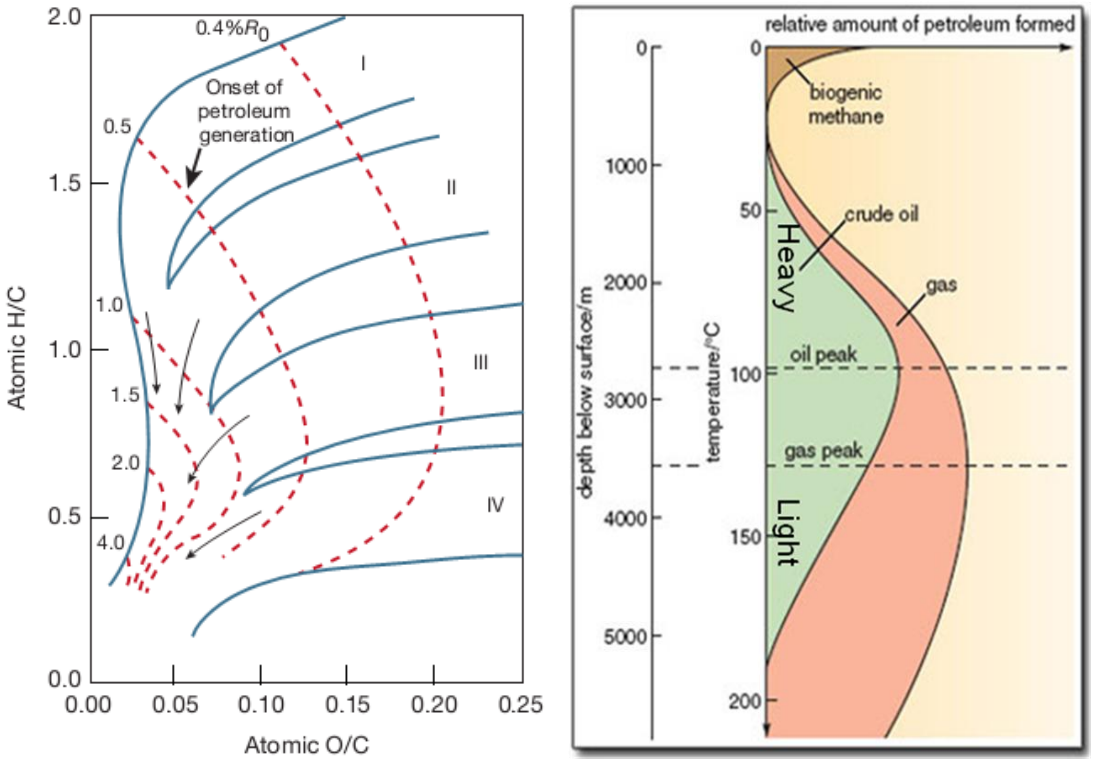

Figure 3.1.2 Chemical evolution of kerogen and petroleum during thermal maturation in sedimentary basins. Left: the chemical evolutions of immature kerogen of various kerogens (type I, II, III, and IV) at increasing levels of thermal maturation. Levels of thermal maturation are indicated by isochors of vitrinite reflectance (%Ro), a widely used geochemical indicator that integrates the effects of time and temperature during thermal maturation of sediments. Generally, kerogen composition moves from the upper right to the lower left in the figure with increasing maturation. Right: the relationship between depth of burial, temperature, and the relative amount of crude oil and natural gas formed from type II kerogen in an area with a geothermal gradient of about 35 ℃/km. (Modified from Seewald, 2003)

3.2 Maturation indicator

Vitrinite is one of the primary components of coal and most sedimentary kerogens. It is typically abundant in type III kerogen-rich source rocks (Figure 3.2.1). With suitable calibration, vitrinite reflectance can be used as an indicator of the level of organic maturity (LOM) in hydrocarbon source rocks by studying the maximum temperature history of sediments in sedimentary basins. Generally, the onset of oil generation is correlated with a reflectance of 0.5 to 0.6 and the termination of oil generation with reflectance of 0.85 to 1.1. The onset of gas generation (the "gas window") is typically associated with values of 1.0 to 1.3 and terminates at around 3.0. However, these generation windows vary among source rocks with different kerogen types (Figure 3.2.1), so a conversion to transformation ratio (TR) can be applied to create a kerogen-specific maturity parameter. The vitrinite reflectance value represents the highest temperature that the vitrinite maceral (and source rock) has experienced, and it is routinely used in 1D burial modeling to identify geological unconformities in sedimentary sections. Typically, vitrinite reflectance data are presented in units of %Ro, which is the measured percentage of reflected light from a sample immersed in oil (%Ro = % reflectance in oil).

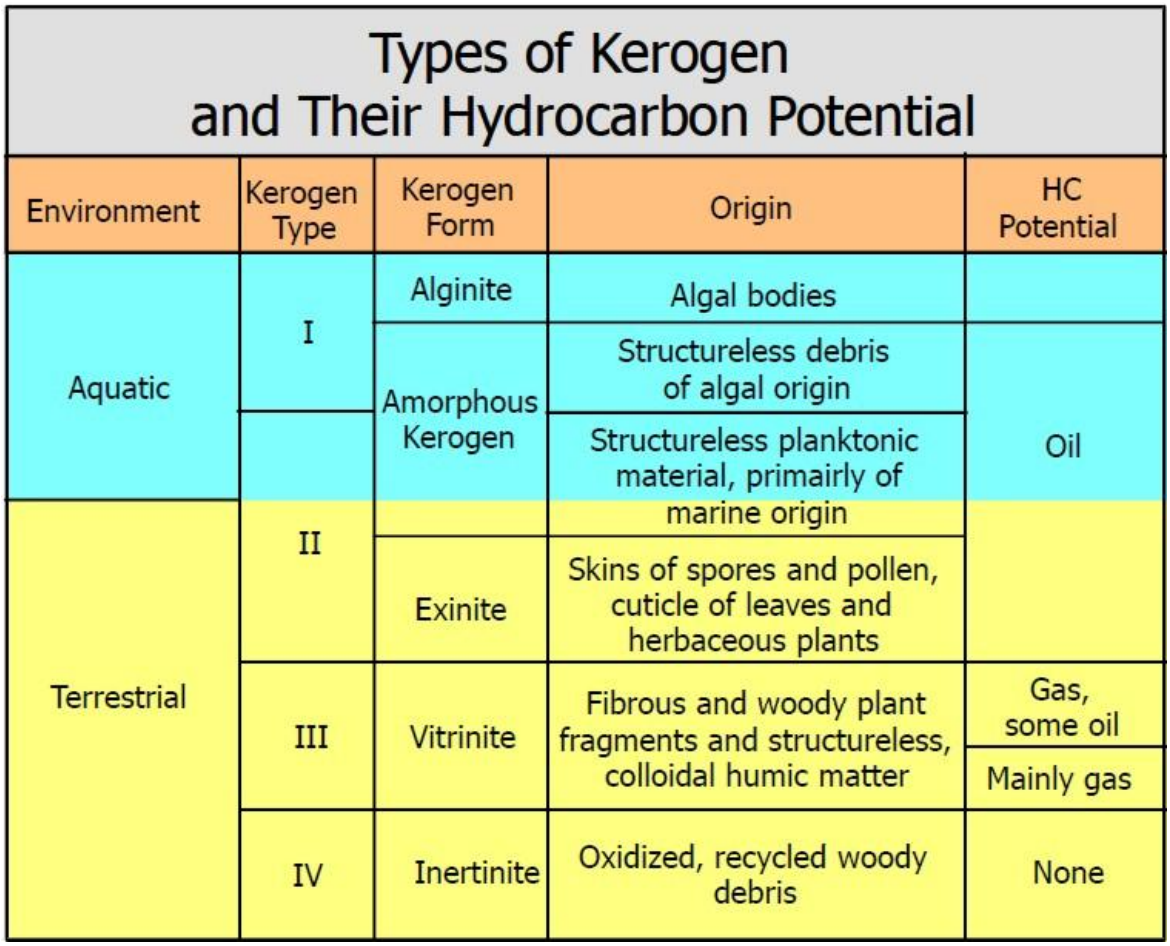

Figure 3.2.1 Types of kerogen and their hydrocarbon potential (Crain, 2011): organic content in gas shale is usually type II.

3.3 Organic matter maturation modeling

To study the properties of organic matter in the source rocks, the amount of kerogen, oil, gas, and residues in various maturation stages are modeled numerically using methods proposed by Luo and Vasseur (1996).

In Figure 3.3.1, the maturation process is divided into three levels. In level I, organic matter can be classified into two categories, generative kerogen and inactive kerogen. The generative part is decomposed gradually into oil, methane, and other gases, including

CO_2, H_2S, and H_2O, which form the gas phase. In level II, with continuing burial, the temperature increases and the liquid hydrocarbon in the sediments decomposes further into the gas phase and solid residue. In level III, at higher temperature, residues generated in the previous level and inactive organic matter can decompose into gas and the final solid product, graphite.

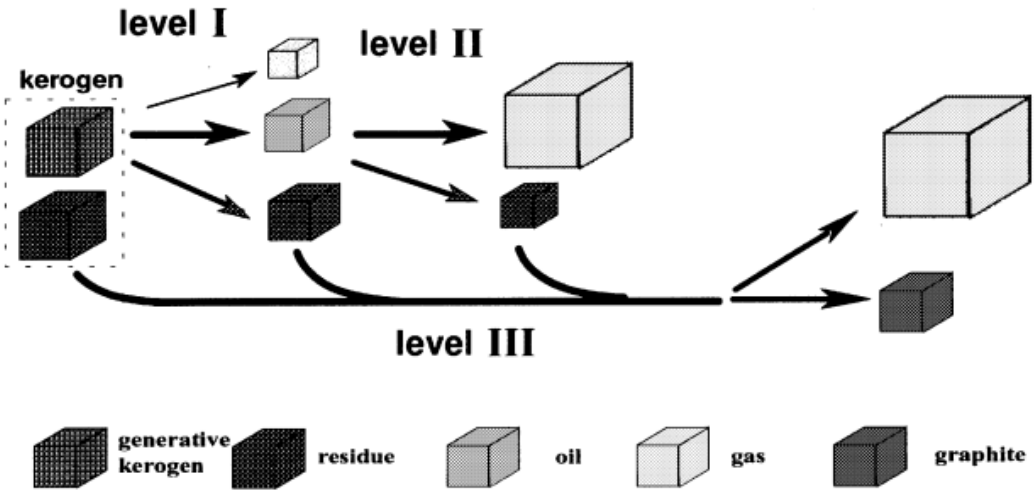

Figure 3.3.1 Simplified model of the maturation of organic matter. Three stages correspond to three transformations, respectively: (1) from kerogen to oil plus gas and residue, (2) from oil to gas plus residue, and (3) from residue to graphite plus gas. (Luo and Vasseur, 1996)

The three decomposition reactions in kerogens are accounted for by a series of first-order chemical reactions calculated with thermal activation. In stage I, the mass of convertible kerogen changes with time t at a rate proportional to its mass:

$$\frac{dM_k}{dt} = -\sum_{j=1}^{6} x_j r_j(t) M_k(t), \qquad (3.3.1)$$

where six parallel reactions are applied (Luo and Vasseur, 1996) and j indicates the j^{th} reaction; $M_k(t)$ is the mass of convertible kerogen at time t; x_j is the initial proportion of

reactant of the j^{th} reaction; and $r_j(t)$ is the reaction rate of the j^{th} reaction, which follows the Arrhenius equation (Carcione and Gangi, 2000); therefore,

$$r_j(t) = A_j e^{-\frac{E_j}{RT(t)}}, \tag{3.3.2}$$

where A_j is the kerogen/oil reaction rate at infinite temperature in the j^{th} reaction and its unit is Ma^{-1}, E_j is the kerogen/oil activation energy in the j^{th} reaction in kJ/mol, R is the gas constant of 8.314 $JK^{-1}mol^{-1}$, and T is the absolute temperature in Kelvin given by

$$T = T_0 + Gz,\ z = St, \tag{3.3.3}$$

where G is the geothermal gradient with a range of 20 to 40 ℃/km, S is a constant sediment burial rate with a range of 0.05 to 0.5 km/Ma, and z and t are the burial depth (km) and age (Ma), respectively. The fraction of kerogen that decomposes to oil is $F_1(t) = [M_{ki} - M_k(t)]/M_{ki}$:

$$F_1(t) = 1 - \sum_{j=1}^{6} \exp[-\int_{t_i}^{t} r_j(t')dt'] \equiv 1 - \sum_{j=1}^{6} \exp[-\Phi_j(t)], \tag{3.3.4}$$

where t_i is the initial time, t is the final time, and $\Phi_j(t)$ is the integral of the j^{th} reaction.

In stage II, oil cracks to form gas, which is modeled by a single kinetic equation (Luo and Vasseur, 1996):

$$\frac{dM_o}{dt} = -r_{og} M_o(t), \tag{3.3.5}$$

where M_o is the mass of oil in sediment. r_{og} is the reaction rate for the conversion of oil to gas and depends on a corresponding preexponential reaction constant A_{og} and the activation energy E_{og}:

$$r_{og}(t) = A_{og} e^{-\frac{E_{og}}{RT(t)}}. \tag{3.3.6}$$

The fraction of oil that decomposes to gas is $F_2(t) = [M_{oi} - M_o(t)]/M_{oi}$:

$$F_2(t) = 1 - \exp[-\int_{t_i}^{t} r_{og}(t')dt'] \equiv 1 - \exp[-\Phi_2(t)]. \tag{3.3.7}$$

In stage III, residues crack to form gas at a higher temperature, which is poorly known but can be modeled by a single kinetic equation (Luo and Vasseur, 1996):

$$\frac{dM_r}{dt} = -r_{rg} M_r(t), \tag{3.3.8}$$

where M_r is the mass of the residues in sediment. r_{rg} is the reaction rate for the conversion of residues cracking to form gas and depends on a corresponding preexponential reaction constant A_{rg} and the activation energy E_{rg}:

$$r_{rg}(t) = A_{rg} e^{-\frac{E_{rg}}{RT(t)}}. \tag{3.3.9}$$

The fraction of oil that decomposes to gas is $F_3(t) = [M_{ri} - M_r(t)]/M_{ri}$:

$$F_3(t) = 1 - \exp[-\int_{t_i}^{t} r_{rg}(t')dt'] \equiv 1 - \exp[-\Phi_3(t)]. \tag{3.3.10}$$

The initial reactant proportions, activation energy, and reaction constants used in organic matter maturation modeling are listed in Table 3.3.1. The assumed weight proportions of the products of the three stages, compiled by Luo and Vasseur (1996), are listed in Table 3.3.2. Geochemists recognize and classify the three types of kerogens by optical and elemental criteria. For example, type I, II, and III kerogen has the highest, the intermediate, and the lowest potential to generate hydrocarbons, respectively.

Table 3.3.1 Parameters used in organic matter maturation modeling.

Kerogen Type	Stage	Reaction Class	x_{init}*	Activation Energy (KJ/mol)	Reaction Constant (Ma^{-1})
I	I	R11	0.024	41.84	4.75×10^{4}
		R12	0.064	125.52	3.04×10^{16}
		R13	0.136	209.20	2.08×10^{25}
		R14	0.152	251.04	3.98×10^{30}
		R15	0.374	292.88	4.47×10^{31}
		R16	1.072	334.72	1.10×10^{34}
	II	R2	1.000	225.94	3.20×10^{25}
	III	R3	1.000	238.49	3.16×10^{26}
II	I	R11	0.022	41.84	1.27×10^{5}
		R12	0.034	125.52	7.47×10^{16}
		R13	0.251	209.20	1.48×10^{27}
		R14	0.152	251.04	5.52×10^{29}
		R15	0.116	292.88	2.04×10^{35}
		R16	0.120	334.72	3.80×10^{35}
	II	R2	1.000	225.94	3.20×10^{25}
	III	R3	1.000	246.86	3.16×10^{26}
III	I	R11	0.023	41.84	5.20×10^{3}
		R12	0.053	125.52	4.20×10^{16}
		R13	0.072	209.20	4.33×10^{25}
		R14	0.091	251.04	1.97×10^{32}
		R15	0.049	292.88	1.20×10^{33}
		R16	0.027	334.72	7.56×10^{31}
	II	R2	1.000	225.94	3.20×10^{25}
	III	R3	1.000	246.86	3.16×10^{26}

*x_{init}: initial reactant proportion

Table 3.3.2 Product weight proportions in various decomposition stages.

Stage	Kerogen Type I			Kerogen Type II			Kerogen Type III		
	Oil	Gas	Residue	Oil	Gas	Residue	Oil	Gas	Residue
I	0.46	0.07	0.47	0.32	0.07	0.60	0.13	0.07	0.80
II	-	0.45	0.55	-	0.45	0.55	-	0.45	0.55
III	-	0.50	0.50	-	0.40	0.60	-	0.30	0.70

Model result

Table 3.3.3 lists some background information, including thicknesses, depths, and ages for several unconventional plays in the U.S., which can be used to set critical parameters (geothermal gradient and sediment burial rate) for the basin model so that the evolution of organic-rich shales can be modeled.

Table 3.3.3 Unconventional plays in the USA.

Unconventional Plays	Thickness (m)	Depth (m)	Age (Ma)	Geological Time	Hydrocarbon
Eagle ford	60-90	1,219-3,660	88-92	Late Cretaceous	Oil and Gas
Haynesville	60-90	3,200-3,962	151-157	Kimmeridgian	Oil and Gas
Barnett	30-300	1,829-2,438	323-354	Mississippian	Oil and Gas
Woodford	36-66	1,829-3,660	~359	Mississippian	Gas
Bakken	0-39	~3,200	~359	Late Devonian-Early Mississippian	Oil and Gas
Marcellus	9-271	0-2,713	383.7-391	Middle Devonian	Gas

For a given constant sediment burial rate, S, of 0.05 km/Ma (Ma = million years), and a constant geothermal gradient, G, of 25 ℃/km, we can model organic-rich shale basin evolution as shown in Figure 3.3.2. The x-axis represents the time since the organic-rich shale reservoir began to be deposited, and the y-axis represents the depth of the organic-

rich shale reservoir, which can be expressed by equation 3.3.3. For every depth and corresponding time, the sediment volume is color-coded with temperature (℃) due to the geothermal gradient. The symbol "*" indicates the onset of hydrocarbon generation, where the corresponding temperature is 50 ℃.

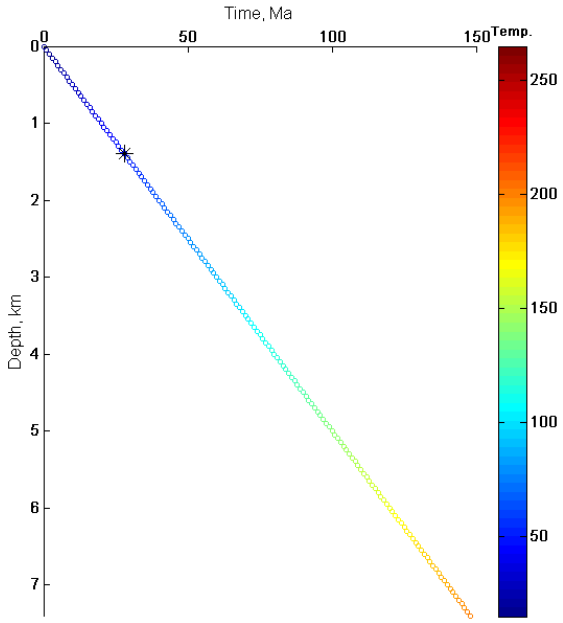

Figure 3.3.2 Basin model of organic-rich shale reservoir. Model parameters: sediment rate S = 0.05 km/Ma, geothermal gradient G = 25 ℃/km.

For most unconventional shale plays in the U.S., kerogen types are classified as type II, with some minor plays belonging to type III. With the aforementioned assumed sediment burial rate and geothermal gradient, we can model conversion fraction in Figure 3.3.3 (left), which can be expressed in equations 3.3.4, 3.3.7, and 3.3.10, and concentrations of various products and initial substances in Figure 3.3.3 (right), which can be calculated by the parameters in Table 3.3.2. From these model results, we find that kerogen starts to

decompose at around 40 Ma (Figure 3.3.3 (left)), which corresponds to the maturation onset symbol "*" in Figure 3.3.2. When the age of the sediment volume is around 90 Ma, generative kerogen finishes maturation, and the rate of kerogen converting to oil gradually decreases to zero. The temperature is over 150 ℃, which corresponds to the schematic in Figure 3.1.2 (right). Oil cracking to form gas happens at around 110 ℃ and finishes at around 180 ℃. Residues and inactive kerogen at a temperature of around 170 ℃ start to crack to form gas and complete decomposition at a temperature of around 220 ℃. The type of hydrocarbon depends on the type of kerogen and its thermal maturity, which will be used to check the feasibility of the following shale maturation models.

Figure 3.3.3 (right) indicates the mass concentration of kerogen, oil, gas, residue, and graphite as final products with the black curve, green circle, red star, black dash, and black hexagram, respectively. This figure quantitatively gives us the mass fractions of various organic matter. When organic matter is immature (before 70 Ma), kerogen, residue, and oil exist in the organic phase. When organic matter is mature (from 70 Ma to 140 Ma), kerogen, residue, oil, and gas may coexist together. When organic matter is overmature (after 140 Ma), kerogen and oil crack completely, and gas, solid residue, and graphite can exist in the space that the initial organic matter takes.

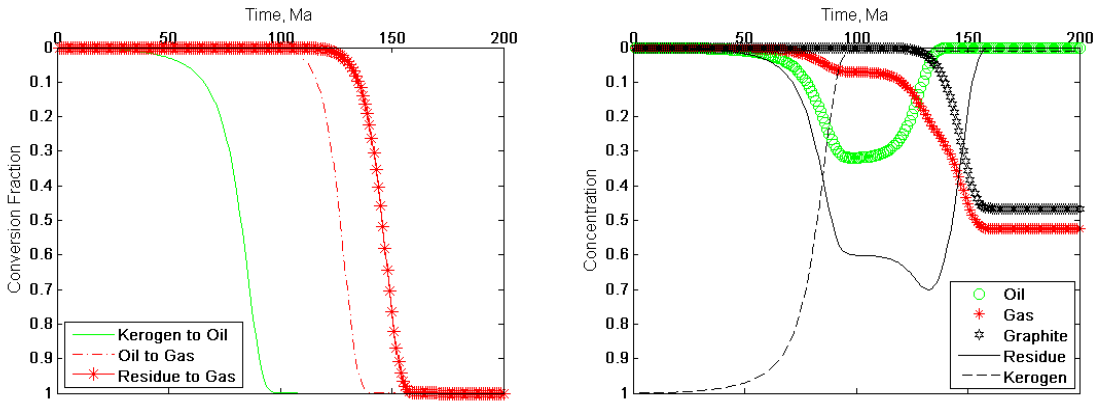

Figure 3.3.3 Left: conversion fraction of kerogen to oil, oil to gas, and residue to gas varying with time. Right: concentration of kerogen, oil, gas, residue, and final graphite. Model parameters: sediment rate S = 0.05 km/Ma, geothermal gradient G = 25 ℃/km, and kerogen type II.

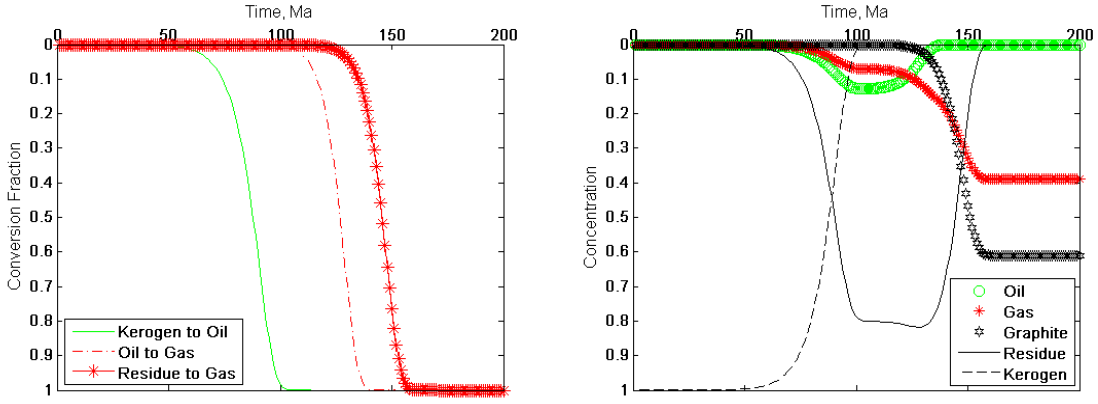

Figure 3.3.4 Left: conversion fraction of kerogen to oil, oil to gas, and residue to gas varying with time. Right: concentration of kerogen, oil, gas, residue and final graphite. Model parameters: sediment rate S = 0.05 km/Ma, geothermal gradient G = 25 ℃/km, and kerogen type III.

Figure 3.3.4 shows the modeled results with the same sediment rate and geothermal gradient but with type III kerogen. In Figure 3.3.4 (left), conversion fractions of type III kerogen to oil, oil to gas, and residue to gas are similar to those of type II shown in Figure 3.3.3 (left), with a tiny difference between the conversion fractions of kerogen to oil. The modeled concentrations in Figure 3.3.4 (right) explain the poorer hydrocarbon

generation potential of type III kerogen compared with type II. The largest gas concentration generated by type II kerogen is about 52%, and the largest gas concentration is about 39% generated by type III.

3.4 Rock physics model

The geophysical characteristics of organic-rich shales remain challenging because of a paucity of understanding of geophysical responses to reservoir properties such as the maturity level and elastic property of organic matter. To describe the fabric of organic-rich shales, an unmanageable number of parameters may be needed. Moreover, investigations and direct measurements of naturally mature samples are confounded by changing mineralogy along with maturity.

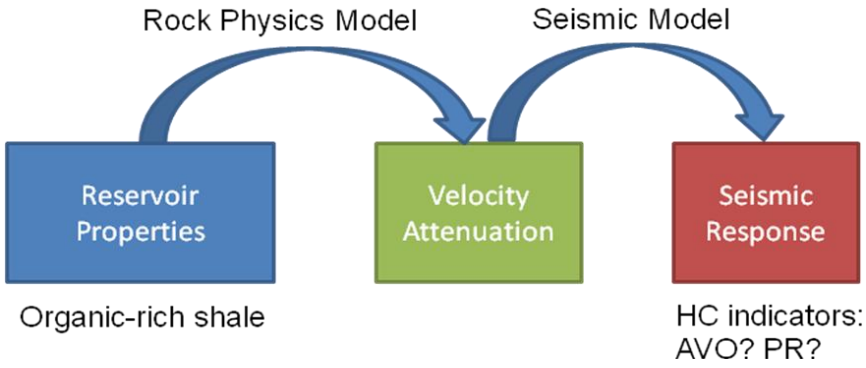

Figure 3.4.1 Schematic of the role that a rock physics model plays in linking microscopic rock properties to seismic responses.

A rock physics model can simplify this problem with reasonable assumptions as well as approximations that help people understand and estimate organic-rich shales' evolution and properties such as elasticity, density, maturity, etc. It can also predict the S-wave

velocity via Vp-Vs relation, which performs well as a lithology and fluid indicator. Despite the existence of quite variable geologic settings, many unconventional plays share features such as heterogeneity, low matrix porosity and permeability, and variations in brittleness. A rock physics model bridges the microscopic reservoir rock properties with macroscopic physical characteristics, such as seismic velocity and attenuation, and it is fundamental in predicting rock/fluid seismic responses through tools such as AVO or Poisson's ratio (Figure 3.4.1). Among numerous factors influencing the properties of organic-rich shales, organic matter is crucial because of the specific velocity, density, and kerogen maturity. At different maturity levels, the properties of kerogen vary and thus affect the properties of the shale matrix: the amount of organic material in the shale decreases during maturation and the shale matrix becomes stiffer (Mba *et al.*, 2010; Prasad *et al.*, 2011); sonic velocities increase and the geomechanic properties of the rock improve at higher maturity.

Many authors have applied different methods to predict and analyze shales' properties. For instance, Carcione *et al.* (2011) found a significant dependence of velocity on total organic content (TOC) when modeling oil-saturated rock using the Backus average as well as the Krief/Gassmann models. Vernik and Milovac (2011), and Zhu *et al.* (2012) found that TOC tends to decrease the P- and S-wave velocities, density, and Vp/Vs ratios, while increasing the velocity anisotropies. Lucier *et al.* (2011) showed that, in the Haynesville shale gas reservoirs, the effect of gas saturation on the Vp-Vs relation is more significant than that of the TOC effects. This implies that TOC predictions from sonic responses are feasible in general, but can be more complicated due to variable pore

fluid compressibility. Guo *et al.* (2013) modeled the Barnett shale brittleness index with self-consistent approximations and the Backus average through considering the degree of the preferred orientation of clay and kerogen particles.

The shale matrix may be considered as a pack of glassy and/or imperfect crystalline grains, sheet-like particles, and amorphous organic matter that is completely or partially compacted. In the matrix, different mineral grains may be discretely located in a continuous or discontinuous mode and may have random or preferred alignments. If a rock matrix contains one continuous and several discontinuous phases, the continuous phase can be treated as the host and the discontinuous phases can be treated as isolated host-embedded inclusions. It is difficult to describe the nature of a rock matrix with a mathematical model due to its complex heterogeneity and properties, such as the volume fractions of various minerals, their stiffness constants, geometry characteristics, and types and degrees of cements.

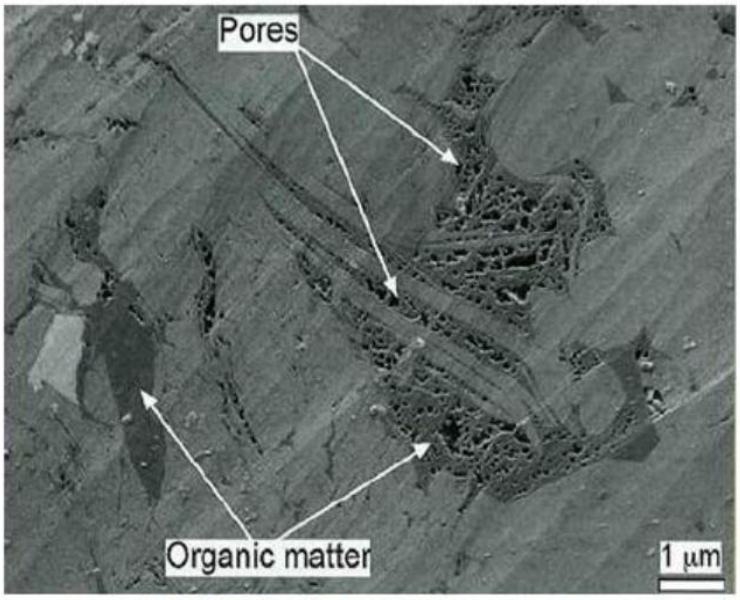

From Robert M. Reed, Bureau of Economic Geology, John A. and Katherine G. Jackson School of Geosciences, The University of Texas at Austin, Austin, TX

Figure 3.4.2 Nano-CT images imply the possibility of two kinds of pore systems in organic-rich shale. The dark part is organic matter coated within the rock matrix. The black pores are maturation-induced micro-cracks filled with hydrocarbons.

Alfred and Vernik (2012) suggested that two kinds of pore systems exist in organic-rich shales: one is kerogen-related pores filled with hydrocarbons, and another is non-kerogen matrix porosity occupied by water (Figure 3.4.2). Ruiz and Azizov (2011a, 2011b) modeled tight shale properties with soft porosity model (SPM) and single aspect ratio (SAR) models. SPM divides the rock's total porosity into two parts: the stiff-pore space (stiff porosity) with an aspect ratio of 1 and the soft-pore space (soft porosity) with an aspect ratio of 0.01. By adjusting their volume fractions, whose sum equals the total porosity, rock behaves with different velocities so that the predicted velocities can match the measured ones. The SAR method assumes that all pores in organic-rich shales share the same aspect ratio. Measured velocities are matched with the model velocities by searching for an effective single aspect ratio (α_{SAR}) of the pores that is required to

accomplish the match. SPM and SAR can both produce good estimations; however, SPM yields more significant consistency with rock microstructure. This thesis uses modified SPM and SAR combined with pore structure as suggested by Alfred and Vernik (2012) to model organic-rich shale rock properties.

Effective medium theory

To model the elastic moduli of organic-rich shales, we consider effective-medium models, which are based on wave scattering theory. Effective medium models are scale-based, and assume that the wavelengths are much larger than the size of the inclusions. Therefore, the wave propagating phenomenon will reflect the overall responses of the rock formation. The effective moduli of mixed grains and pores generally depend on the volume fractions of various phases, the properties of individual components, and the geometry of the spatial distribution of each component. For example, using porosity without specifying the geometry of pore spaces, the bulk and shear moduli of a poro-elastic medium will fall between the Voigt and Reuss bounds or the Hashin-Shtrikman (1963) bounds. If pore geometry information is included, rock's effective moduli can be calculated precisely. The self-consistent approximation (SCA) method (Berryman, 1980; 1995) and the differential effective medium (DEM) approximation (Norris, 1985) are applied at different steps in a rock model, and they both satisfy the Hashin-Shtrikman bounds, which offer us the narrowest possible range without specifying anything about the geometry of the constituents. For these two effective medium model methods, cracks are isolated with respect to fluid flow. Pore pressures are unequilibrated, and they both

are appropriate for high-frequency laboratory conditions for sandstone or even for seismic frequencies for shale.

Self-consistent approximation

The self-consistent approximation (Budiansky, 1965; Hill, 1965; Wu, 1966) can add higher concentrations of inclusions into the effective medium than can the Kuster and Toksöz model (1974). The self-consistent approximation (SCA) method solves effective medium properties by assuming an as-yet-unknown property (Poisson's ratio, for instance) and replaces the background medium property with the as-yet-unknown effective medium. This iteration does not stop until the difference between the effective medium properties is solved by the iterative methods and the solutions are small enough. The equations for the effective bulk and shear moduli, K_{SC}^{*} and μ_{SC}^{*}, of a cracked medium with N-phase composites (Berryman, 1980, 1995) are:

$$\sum_{i=1}^{N} x_i (K_i - K_{SC}^{*}) P^{*i} = 0, \tag{3.4.1}$$

$$\sum_{i=1}^{N} x_i (\mu_i - \mu_{SC}^{*}) Q^{*i} = 0, \tag{3.4.2}$$

where i refers to the i^{th} material, x_i is its volume fraction, P and Q are geometric factors, and the superscript *i on P and Q (Table 3.4.1) indicates that the factors are for an inclusion of material i in a background medium with self-consistent effective moduli K_{SC}^{*} and μ_{SC}^{*}.

Table 3.4.1 Coefficients P and Q for some specific shapes. The sub-scripts m and i refer to the background and inclusion materials (Berryman, 1995).

Inclusion shape	P^{mi}	Q^{mi}
Spheres	$\frac{K_m + \frac{4}{3}\mu_m}{K_i + \frac{4}{3}\mu_m}$	$\frac{\mu_m + \frac{4}{3}\zeta_m}{\mu_i + \frac{4}{3}\zeta_m}$
Needles	$\frac{K_m + \mu_m + \frac{1}{3}\mu_i}{K_i + \mu_m + \frac{1}{3}\mu_i}$	$\frac{1}{5}\left(\frac{4\mu_m}{\mu_m + \mu_i} + 2\frac{\mu_m + \gamma_m}{\mu_i + \gamma_m} + \frac{K_i + \frac{4}{3}\mu_m}{K_i + \mu_m + \frac{1}{3}\mu_i}\right)$
Disks	$\frac{K_m + \frac{4}{3}\mu_i}{K_i + \frac{4}{3}\mu_i}$	$\frac{\mu_m + \frac{4}{3}\zeta_i}{\mu_i + \frac{4}{3}\zeta_i}$
Penny cracks	$\frac{K_m + \frac{4}{3}\mu_i}{K_i + \frac{4}{3}\mu_i + \pi\alpha\beta_m}$	$\frac{1}{5}\left(1 + \frac{8\mu_m}{4\mu_i + \pi\alpha(\mu_m + 2\beta_m)} + 2\frac{K_i + \frac{2}{3}(\mu_i + \mu_m)}{K_i + \frac{4}{3}\mu_i + \pi\alpha\beta_m}\right)$

Notes:

$\beta = \mu\frac{3K+\mu}{3K+4\mu}$, $\gamma = \mu\frac{3K+\mu}{3K+7\mu}$, $\zeta = \frac{\mu}{6}\frac{9K+8\mu}{(K+2\mu)}$, *α: crack aspect ratio, a disk is a crack of zero thickness.*

The summations cover all phases containing minerals and pores. Dry cavities can be modeled by setting the inclusion moduli to zero. Fluid-saturated cavities are computed by setting the inclusion shear moduli to zero.

Differential effective medium

The differential effective medium (DEM) theory models a two-phase composite by incrementally adding inclusions of one phase to the matrix phase (Cleary *et al.*, 1980; Norris, 1985; Zimmerman, 1991). DEM does not treat each constituent symmetrically. It starts with material 1 as the host and incrementally adds material 2 as an inclusion of

material l. Therefore, for multiple inclusion shapes or multiple constituents, the effective moduli depend not only on the final volume fractions of the constituents but also on the order in which the incremental additions are added. Materials often have the characteristic of connectivity, and a rock matrix can be treated as a host, while pores filled with fluid or kerogen can be treated as inclusions. If the selected materials have microstructures that are consistent with the DEM methods, DEM provides consistently accurate predictions over a wide range of volumetric concentrations and with a fairly narrow range of aspect ratios (Ruiz, 2009). The DEM models higher velocities or stiffer moduli than the SCA method. The coupled system of ordinary differential equations for the effective bulk and shear moduli, K^* and μ^*, respectively, are (Berryman, 1992):

$$(1-y)\frac{d}{dy}[K^*(y)] = (K_2 - K^*)P^{(*2)}(y), \tag{3.4.3}$$

$$(1-y)\frac{d}{dy}[\mu^*(y)] = (\mu_2 - \mu^*)Q^{(*2)}(y), \tag{3.4.4}$$

with initial conditions $K^*(0) = K_1$ and $\mu^*(0) = \mu_1$, where K_1 and μ_1 are the bulk and shear moduli of the initial host material (phase 1), K_2 and μ_2 are the bulk and shear moduli of the incrementally added inclusions (phase 2), and y is the concentration of phase 2. P and Q terms are geometric factors in Table 3.4.1, and superscript *2 on P and Q indicates that the factors are for an inclusion of material 2 in a background medium with effective moduli K* and μ*.

Anisotropies induced by oriented cracks filled with fluid or clay minerals were calculated by Nishizawa (1982) and Hornby *et al.* (1994) by extending the self-consistent

approximation (SCA) and differential effective medium (DEM) methods into an anisotropic version. The elastic field of an ellipsoidal inclusion in a homogeneous host is solved to simulate induced heterogeneity.

In the following sections, rock physics models are built for immature, mature, and overmature shales based on organic-rich shales' evolution history. Different parameters are applied with suitable physical meaning. For the immature and mature organic-rich shale models, the Bakken shale core data from Vernik and Nur (1992) are taken as a reference.

Step I: the fully aligned clay-fluid composite

We start by generating anisotropic clay-fluid structures. Clay mineral particles are featured as hexagonal symmetry, and their properties (elasticity and density) are compiled in Table 3.4.2.

Table 3.4.2 Clay mineral elastic properties used in this thesis.

Authors	Source	C_{11} (GPa)	C_{33} (GPa)	C_{55} (GPa)	C_{66} (GPa)	C_{13} (GPa)
Carcione *et al.* (2011)	Bakken illite mineral	65.0	52.7	21.9	25.8	38.5
Sayers (2013)	Ulm and Abousleiman (2006); Ortega, Ulm, and Abousleiman (2007)	44.9	24.2	3.7	11.6	18.1
Sayers (2013)	Crystallographic structure and composition of illite/muscovite from Tosaya (1982)	178	54.9	12.2	42.4	14.5

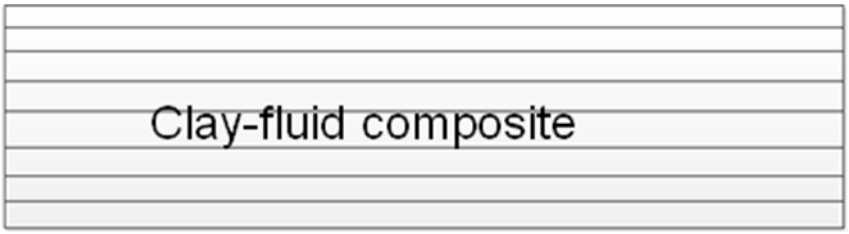

Figure 3.4.3 Schematic of clay-fluid composite. Clay-related pores are oriented in alignment.

To create a biconnected solid at specific porosities (Figure 3.4.3), we can use an anisotropic version of the differential effective medium (DEM) method. This is because, in the evolution history of organic-rich shales, clay minerals aggregate (suspension status) and start to be deposited with time, and the degree of compaction increases with time, leading to decreased porosity. We assume that the fluid in clay-related pores is water. The DEM helps to preserve the connectivity of the clay solid phase, and pore-filled water is treated as non-connected phase (inclusions) due to the low permeability of organic-rich shales as well as its unequilibrated pore pressure, even if seismic-frequency waves pass through. In this thesis, the aspect ratios of clay-related pores are calculated with a single aspect ratio (SAR) model ($0.01 < \alpha < 1$) and can be interpreted using the relationship between pore shape and compaction. Hereby, we neglect the smectite-to-illite transformation during shales compaction. By applying the known properties of water (K_w = 2.25 GPa, μ_w = 0 GPa, ρ_w = 1.04 g/cc) and clay mineral, we can generate clay-fluid composite properties.

Step II: include silt minerals in the generated clay-fluid composite

Silt-sized minerals (quartz, feldspar, calcite, and pyrite) tend to exist as roughly spherical shapes that are randomly oriented, and their concentrations vary in local unconventional shale plays. We can use anisotropic self-consistent approximation (SCA) to include silt-sized minerals in clay-fluid composites to obtain the elastic properties of shale's inorganic part, as it is unnecessary to identify one of the minerals as the host and the other two as inclusions (Figure 3.4.4).

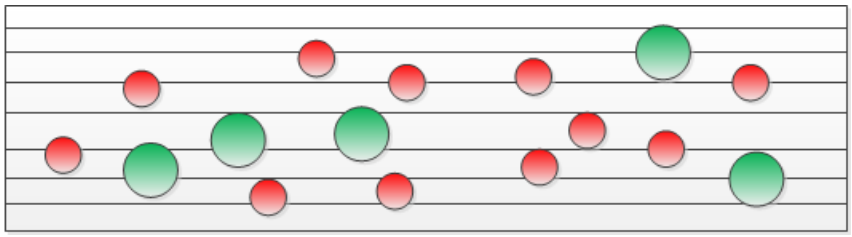

Figure 3.4.4 Schematic of adding silt minerals into anisotropic clay-fluid composites.

Step III: model organic matter properties with different maturity levels

Normally, in immature shale, its porosity is close to 0, so its grain density is inversely correlated with the total organic carbon (TOC) and the grain density can be smaller than 2.2 g/cc when TOC is high. For cooked shale (the mature case), which has experienced high temperature and pressure, its porosity is intermediate (~5%), and TOC is low. For overcooked shale (the overmature case), which has a low Vp/Vs ratio due to the large amount of gas; there is no oil or water in the pores, and TOC correlates with porosity. The key issue in modeling organic-rich shales is to the model appropriate properties of organic matter.

In the process of organic matter maturation, various reactions take place at different maturity levels. Three models are built based on different maturity levels (immature, mature, and overmature), where different values of the elastic properties of kerogen and the geometry of kerogen-related pores based on their aspect ratio are selected. The properties of organic matter properties are closely related with its maturation. Many authors have reported that the more mature organic matter is, the stiffer and denser the kerogen becomes. For example, Yan and Han (2012) performed an ultrasonic measurement of cored kerogen that was retrieved and processed from the Green River Shale in Colorado. For immature kerogen, its bulk moduli vary from 3.5 to 5 GPa, and its shear moduli are about half of that. Lucier *et al.* (2011) applied a bulk modulus of 7.98 GPa and a shear modulus of 4.18 GPa when modeling the Haynesville gas shale, which is in the overmature stage and whose Ro (%) ranges from 2.0 to 2.8. Alfred and Vernik (2012) proposed a trend, expressed with regression equation 3.4.5,

$$\rho_k = 1.293 R_o^{0.2}, \tag{3.4.5}$$

between different vitrinite reflectance (Ro, %) and kerogen density through studying core data (Figure 3.4.5). Because of the deeper burial environment, with an increasing degree of maturity, more kerogen-related pores are generated, which can be quantified with the kerogen-related porosity for immature, mature, and overmature cases. As the maturity level increases, more kerogen-related pores are generated and they can connect, and the rock becomes loaded with greater vertical stress at greater depth, which may even close

the generated kerogen-related pores. Thus, the aspect ratio of kerogen-related pores can decrease with increasing maturity level.

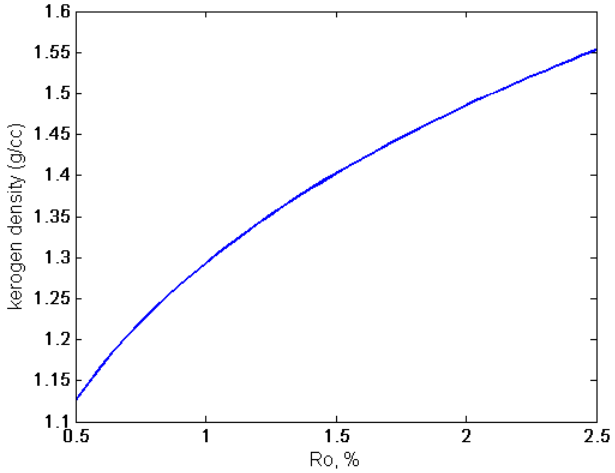

Figure 3.4.5 The relationship between the density of kerogen and vitrinite reflectance.

Figure 3.4.6 Schematic of organic matter consisting of kerogen and kerogen-related pores produced during kerogen maturation.

Here, we treat organic matter as a system consisting of solid kerogen or a mixture of residue with graphite, as well as kerogen-related pores filled with hydrocarbons (Figure 3.4.6) distributed in the organic matter. The substance phases and their volume fractions in the organic matter depend on the organic-rich shale basin model built in the last section (Figure 3.3.3 (right) and Figure 3.3.4 (right)). Since we can treat the organic system as an effective medium, the cracked kerogen elastic properties can be calculated using the self-consistent approximation (SCA) method. For immature kerogen (Ro (%) <

0.6) (Vanorio *et al.*, 2008), a bulk modulus of 3.5 GPa and a shear modulus of 1.75 GPa are applied. In this stage, the temperature of the formation is below 60 ℃, and little gas and few kerogen-related pores are generated. For mature kerogen (0.6 < Ro (%) < 1.3), pore fluid can be treated as a mixture of oil and gas, whose stiffness is calculated with Wood's (1955) relation, and the bulk and shear moduli of solid kerogen are 5 GPa and 2.5 GPa, respectively. For overmature kerogen (Ro (%) > 1.3), the elastic properties of a solid mixture of kerogen and graphite can be calculated using the SCA method since we can suggest reasonable aspect ratios for these two materials based on the microstructure observed from SEM images. Furthermore, all the oil decomposes to form gas because of the higher temperature (> 150 ℃), and the fluid in kerogen-related pores and matrix pores is only gas. The elastic moduli of kerogen (Lucier *et al.*, 2011) and graphite (Ruiz, 2009) are set at 7.98 GPa and 4.18 GPa and 4.79 GPa and 4.54 GPa, respectively. Table 3.4.3 lists the elastic properties, hydrocarbon types, kerogen-related pore properties and aspect ratios for three different maturity levels and inorganic solid carbon-phase graphite.

Table 3.4.3 Materials elastic properties and kerogen-related pore properties utilized in the organic-rich shale model.

Material	Hydrocarbon Types	K (GPa)	μ (GPa)	Ro (%)	Kerogen-Related Porosity	Aspect Ratio
Immature kerogen	Oil	3.5	1.75	<0.6	<0.5%	0.5
Mature kerogen	Oil and Gas	5	2.5	0.6<Ro<1.3	1%-8%	0.2
Overmature kerogen	Gas	7.98	4.18	>1.3	1%-5%	0.1
Graphite	-	4.79	4.54	-	-	0.1

Step IV: add organic matter in the former shale background

After we generate the effective properties of organic matter with different maturity levels, we can add cracked kerogen as an inclusion in the former shale matrix to simulate the properties of organic-rich shale. In this step, the cracked kerogen serving as isolated inclusions is assumed to be aligned along the shale bedding (Figure 3.4.7). To preserve the connectivity of the rock matrix, an anisotropic version of the DEM method is applied.

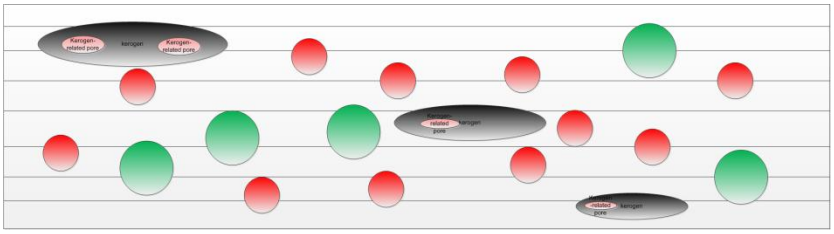

Figure 3.4.7 Schematic of added organic matter as inclusions into former shale background.

Step V: average over the orientation distribution function

The structure of shale in Figure 3.4.8 shows that the clay aggregates' alignment varies in orientation but serves as a transverse isotropic (TI) medium as a whole, whose symmetry axis is perpendicular to the formation. Hornby *et al.* (1994) described the properties of the composite in terms of a complex solid comprised of a distribution of these particle aggregates. This thesis adopts this averaging strategy to add a particle distribution characteristic into the organic-rich shale model (Figure 3.4.9).

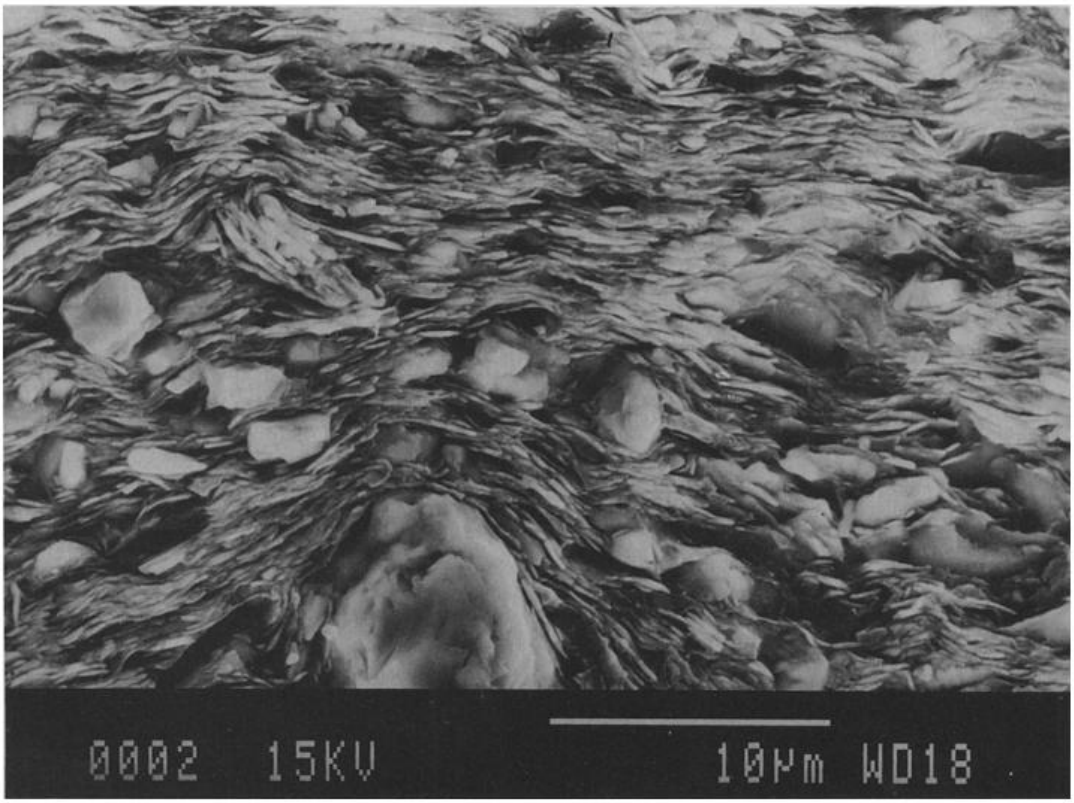

Figure 3.4.8 A scanning electron microscope (SEM) image of shale. The sheet-like particles are clay minerals, while the larger, nearly spherical particles are silt. (Hornby, 1994)

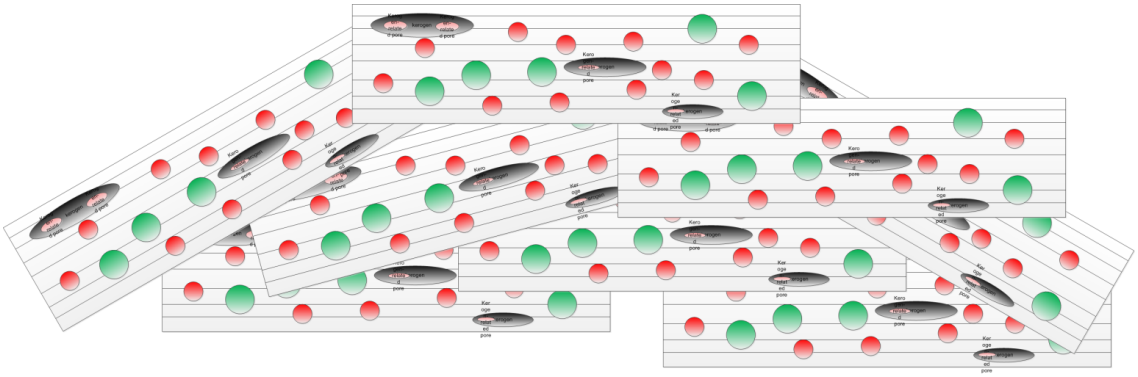

Figure 3.4.9 Schematic of averaging over the particle orientation distribution function to generate organic-rich shale composites.

Three steps are required to compute the averaging particle orientation distribution. First, we calculate the stiffness and compliance tensors for each polar angle θ between the clay

aggregates' symmetry axis and the overall symmetry axis of the formation and each azimuthal angle ϕ, which is the horizontal angle between the clay aggregates and the overall formation. The initial rotation around one of the TI medium's symmetry axes (the polar angle rotation) is achieved by the following transformation:

$$c^*_{ijkl}(\theta,0) = L_{im}L_{jn}L_{kp}L_{lq}c^*_{mnpq}(0,0), \tag{3.4.6}$$

where

$$L_{ij} = \begin{bmatrix} 1 & 0 & 0 \\ 0 & \cos\theta & -\sin\theta \\ 0 & \sin\theta & \cos\theta \end{bmatrix}. \tag{3.4.7}$$

Then we can calculate the stiffness tensor after rotating the TI medium azimuthally in the horizontal plane:

$$c^*_{ijkl}(\theta,\phi) = L_{im}L_{jn}L_{kp}L_{lq}c^*_{mnpq}(\theta,0), \tag{3.4.8}$$

and the transformation tensor is given by

$$L_{ij} = \begin{bmatrix} \cos\phi & -\sin\phi & 0 \\ \sin\phi & \cos\theta & 0 \\ 0 & 0 & 1 \end{bmatrix}. \tag{3.4.9}$$

In the above equations, their subscripts (i, j, k, and l and m, n, p, and q) follow Einstein's summation convention. $c^*_{ijkl}(\theta,\phi)$ is the tensor of the effective stiffness of the aligned shale matrix subcrystals whose symmetry axis are rotated by the polar angles θ and the azimuthal angles ϕ. Similarly, the compliance tensor $s^*_{ijkl}(\theta,\phi)$ is solved for rotation by the polar angles θ and the azimuthal angles ϕ for the shale matrix compliance tensor.

Second, the rotated stiffness and compliance tensors of all the cases are averaged over the orientation distribution function D(θ), which describes the angle distribution between the subcrystal symmetry axis and the composite formation symmetry axis:

$$\int_{-\pi/2}^{\pi/2} D(\theta) d\theta = 1, \tag{3.4.10}$$

For numerical calculations, in a TI medium, it is sufficient to rotate the tensors $c_{ijkl}^{*}(\theta,\phi)$ and $s_{ijkl}^{*}(\theta,\phi)$ by a series of successive rotations and average the results. θ varies from –π/2 to π/2 with an interval of π/4, and ϕ varies from 0 to 5π/3 in increments of π/3. We can use equations 3.4.11 and 3.4.12 to average the effective stiffness and compliance:

$$\underset{\sim}{C}^{V} = \frac{1}{6}\sum_{n=1}^{N}\sum_{i=1}^{6} D(n)\underset{\sim}{C}^{*}(n,\phi_i), \tag{3.4.11}$$

$$\underset{\sim}{S}^{R} = \frac{1}{6}\sum_{n=1}^{N}\sum_{i=1}^{6} D(n)\underset{\sim}{S}^{*}(n,\phi_i), \tag{3.4.12}$$

where $\underset{\sim}{C}^{V}$,and $\underset{\sim}{S}^{R}$ are the composite stiffness and compliance tensors, respectively; $\underset{\sim}{S}^{*}(n,\phi_i) = [\underset{\sim}{C}^{*}(n,\phi_i)]^{-1}$ is the effective compliance for the aligned particle aggregates.

Third, the Voigt-Reuss-Hill (VRH) average (Hill, 1952) is applied to simulate the comprehensive effect of averaging through the stiffness and compliance tensors. The rock stress distribution is assumed to follow the VRH average in equation 3.4.13:

$$\underset{\sim}{C}^{VRH} = \frac{\underset{\sim}{C}^{V} + (\underset{\sim}{S}^{R})^{-1}}{2}. \tag{3.4.13}$$

The above rotations are governed by a distribution D(θ), which is derived from an SEM image by Hornby *et al.* (1994). In our organic-rich shale models, these particles' orientation distribution function adopts a discrete normal distribution.

3.5 Rock physics model results and analysis

Immature model

The Bakken shale ultrasonic measurements from Vernik and Nur (1992) are used to investigate the predictive power of the immature model and the mature model. Available vitrinite reflectance data for the Bakken shale samples from Vernik (1994) help us divide 11 samples into two categories: three immature samples with Ro (%) < 0.6 and eight mature samples with 0.6 < Ro (%) < 1.3. Vernik and Milovac (2011) suggested that the clay content (predominantly illite) in organic-rich shales at the Bakken and Woodford formations ranges from 20% to 25% in more siliceous and carbonate-rich shales. With a combination of an inorganic matrix mineral volume fraction of 40% quartz, 35% calcite, and 25% clay and other parameters listed in Table 3.5.1, we simulate organic-rich shales' properties with varying kerogen volume fraction (VTOC) from 5% to 45%. Figures 3.5.1 to 3.5.4 demonstrate the modeled results with colored dots and the measured data with red stars. A kerogen density of 1.1 g/cc is applied.

Table 3.5.1 Parameters used in the immature organic-rich shale model.

Matrix porosity (ϕ_{nk})	0.7%	**K_{oil}**	0.57 GPa
Matrix-related pore aspect ratio (α_{nk})	0.1	**μ_{oil}**	0 GPa
Kerogen-related porosity (ϕ_k)	0-0.5%	**ρ_{oil}**	0.9 g/cc
Kerogen-related pore aspect ratio (α_k)	0.5	**K_{water}**	2.25 GPa
Kerogen mineral aspect ratio ($\alpha_{kerogen}$)	0.1	**μ_{water}**	0 GPa
Clay mineral aspect ratio (α_{clay})	0.1	**ρ_{water}**	1.04 g/cc

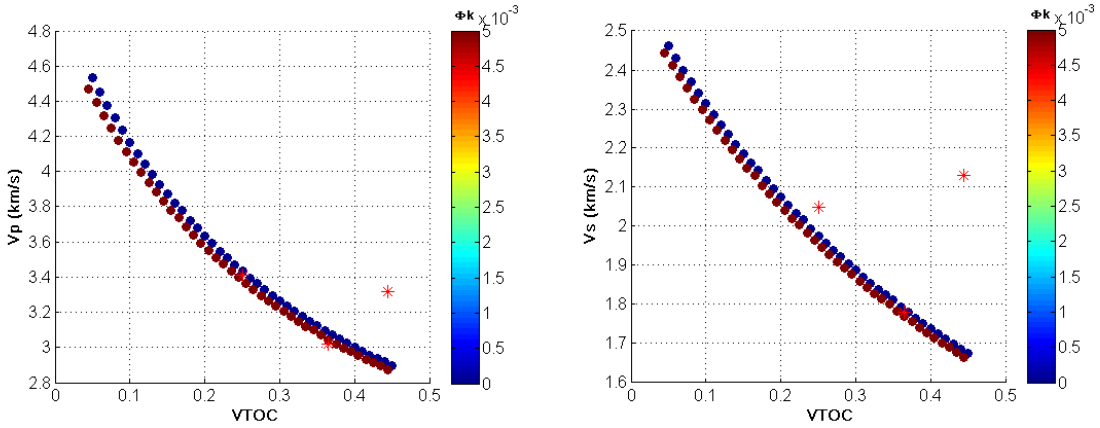

Figure 3.5.1 Left: immature organic-rich shale rock physics model: P-wave velocity (Vp) vs. kerogen volume fraction (VTOC). Right: immature organic-rich shale rock physics model: S-wave velocity (Vs) vs. kerogen volume fraction (VTOC). Red stars indicate the Bakken shale data with Ro (%) < 0.6 from Vernik and Nur (1992).

Figure 3.5.1 shows us that the modeled P- and S-wave (normal-to-bedding) velocities will decrease with increasing TOC because TOC is much softer than other minerals. The kerogen-related porosities ϕ_k are tiny because in the immature case or in oil shale, little kerogen decomposes to form oil and few kerogen-related pores are generated. For the same values of kerogen volume, the generation of kerogen-related pores will lower both the P- and S-wave velocities as well as the total volume of kerogen. The total porosities can be calculated using the sum of the kerogen-related porosities ϕ_k and a matrix

porosity of 0.7%. The Bakken shale data with Ro (%) < 0.6 from Vernik and Nur (1992) are plotted and marked with red stars.

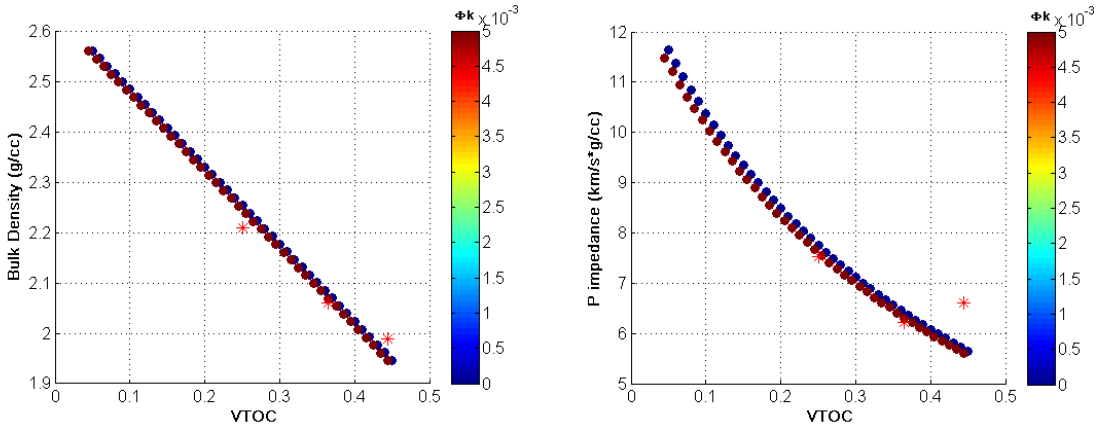

Figure 3.5.2 Left: immature organic-rich shale rock physics model: bulk density vs. kerogen volume fraction (VTOC). Right: immature organic-rich shale rock physics model: P- wave impedance vs. kerogen volume fraction (VTOC). Red stars indicate the Bakken shale data with Ro (%) < 0.6 from Vernik and Nur (1992).

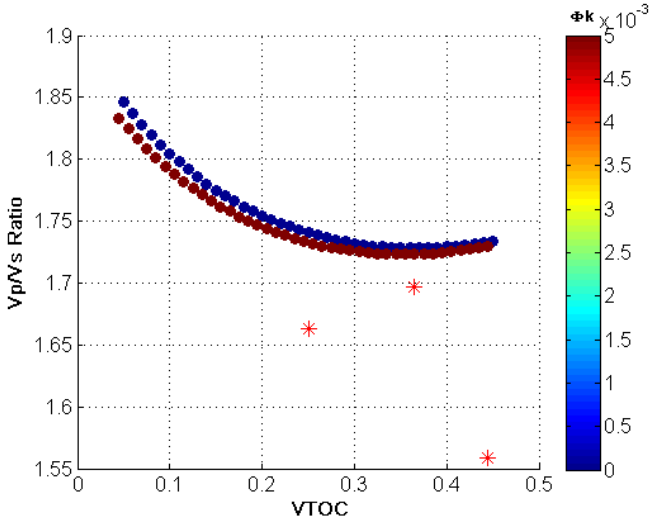

Figure 3.5.3 Immature organic-rich shale rock physics model: Vp/Vs ratio vs. kerogen volume fraction (VTOC). Red stars indicate the Bakken shale data with Ro (%) < 0.6 from Vernik and Nur (1992).

It is verified that the bulk density is highly correlated with kerogen volume due to the low total porosities (< 1%), as shown in Figure 3.5.2. They follow the trend well for Vp-VTOC, Vs-VTOC, bulk density-VTOC, and P-impedance-VTOC except for the core data points with a kerogen volume fraction of 43%. For that core sample, the Vp/Vs value in Figure 3.5.3 is as low as that of gas sand; however, at such a maturity level (Ro = 0.3%), the accuracy of this measurement is questionable, and we do not know the pore fluid saturation. With a higher amount of kerogen (VTOC > 25%), the Vp/Vs ratio of organic-rich shale is close to 1.73 and does not change significantly. When the kerogen amount is lower (VTOC < 25%), the higher the kerogen volume is, the lower the Vp/Vs ratio of organic-rich shale is.

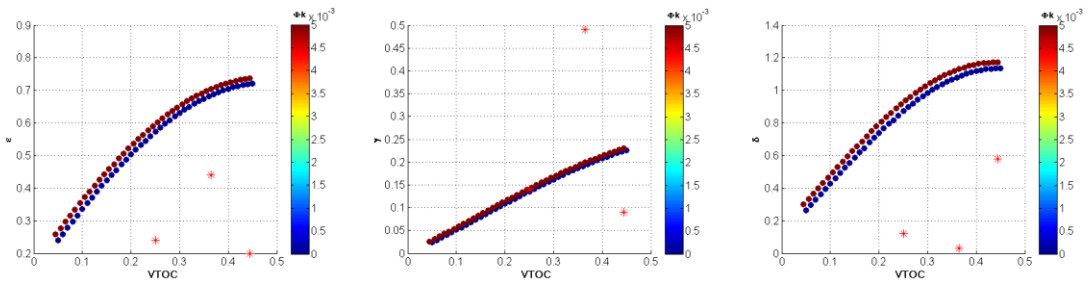

Figure 3.5.4 Thomsen's parameters varying with volumes of kerogen and kerogen-related porosities. Left: ε vs. kerogen volume fraction (VTOC). Middle: γ vs. kerogen volume fraction (VTOC). Right: δ vs. kerogen volume fraction (VTOC). Red stars indicate the Bakken shale data with Ro (%) < 0.6 from Vernik and Nur (1992).

Normally, kerogen is treated as isotropic material, but its alignment can induce stronger polar anisotropy. Figure 3.5.4 demonstrates that, with increasing organic matter, more kerogen particles are aligned parallel to the bedding plane, and the Thomsen's parameters (Thomsen, 1986) increase. The reason for the overestimation of anisotropies may be missing microstructure information of particle alignments or lower aspect ratios for some

inclusions, such as clay minerals, kerogen, etc., which will increase the difference between the stiffness constants along and normal to the bedding.

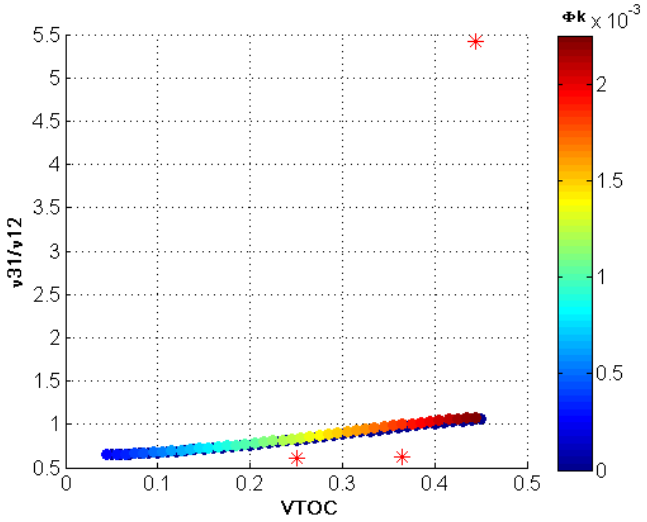

Figure 3.5.5 Immature organic-rich shale rock physics model: ν_{31}/ν_{12} ratio vs. kerogen volume fraction (VTOC). Red stars indicate the Bakken shale data with Ro (%) < 0.6 from Vernik and Nur (1992).

Poisson's ratios in the TI medium can provide us with strategies when studying rock mechanic properties such as brittleness. Carcione and Cavallini (2002) used ν_{31} and ν_{13} to indicate abnormal pore pressure, and Sayers (2013) suggested that $\nu_{31} < \nu_{12}$ may indicate the existence of microcracks in the organic-rich shales. Figure 3.5.5 shows the modeled relationship between the ν_{31}/ν_{12} ratio and kerogen volume fractions (VTOC). When the kerogen volume fraction is below 35%, the ν_{31}/ν_{12} ratio is less than 1. However, with an increasing amount of organic matter, the ν_{31}/ν_{12} ratio can be larger than 1. Still, the ν_{31}/ν_{12} ratio of core data with a kerogen volume of 43% is abnormally high, which is questionable at low vitrinite reflectance.

Mature model

Compared with immature organic-rich shales, organic matter becomes denser and stiffer. The kerogen bulk and shear moduli are set at 5 GPa and 2.5 GPa, respectively, and a density of 1.3 g/cc is applied. At the same time, more kerogen cracks to form oil and gas. Therefore, since the pore fluids in the kerogen-related pores consist of oil and gas, the hydrocarbon system's elastic properties can be calculated using Wood's equation (Reuss Bound). As shown in Figure 3.3.3 (right), for type II kerogen, when organic-rich shale is mature (around 70 to 80 Ma), the mass concentrations of the organic phase are 70% solid organic matter, 20% oil, and 10% gas. Kerogen and residue generated during kerogen cracking to form oil and gas are assumed to share the same elastic properties and density but different reaction activity energy. The inorganic matrix of our model consists of a mineral combination of 25% quartz, 55% calcite, and 20% clay. The matrix porosity is 1%, and kerogen-related porosities vary from 0% to 8%, which are correlated with crack densities varying from 0 to 0.2 in equation 4.4.14:

$$\varepsilon = \frac{N}{V} a^3 = \frac{3\phi}{4\pi\alpha}, \tag{4.4.14}$$

where ε is the crack density, N/V is the number of penny-shaped cracks of radius a per unit volume, and ϕ and α are the crack porosity and aspect ratio, respectively. Other parameters used in the mature organic-rich shale model are listed in Table 3.5.2. We simulate mature organic-rich shales' properties with changing kerogen volume fractions (VTOC) ranging from 5% to 45%. Figures 3.5.6 to 3.5.9 demonstrate the modeled results and eight mature Bakken shale samples from Vernik (1994) with vitrinite reflectance

(Ro, %) varying from 0.6 to 1.1 used to check the feasibility and physics of the built model.

Table 3.5.2 Parameters used in the mature organic-rich shale model.

Matrix porosity (ϕ_{nk})	1%	**K_{oil}**	0.48 GPa
Matrix-related pore aspect ratio (α_{nk})	0.1	**μ_{oil}**	0 GPa
Kerogen-related porosity (ϕ_k)	0-8%	**ρ_{oil}**	0.8 g/cc
Kerogen-related pore aspect ratio (α_k)	0.2	**K_{water}**	2.25 GPa
Kerogen mineral aspect ratio ($\alpha_{kerogen}$)	0.1	**μ_{water}**	0 GPa
Clay mineral aspect ratio (α_{clay})	0.1	**ρ_{water}**	1.04 g/cc
Gas to oil volume ratio in kerogen related pores	9	**K_{gas}**	0.01 GPa
Crack density (ε)	0-0.2	**μ_{gas}**	0 GPa
Initial amount of kerogen volume fraction	5%-45%	**ρ_{gas}**	0.1 g/cc

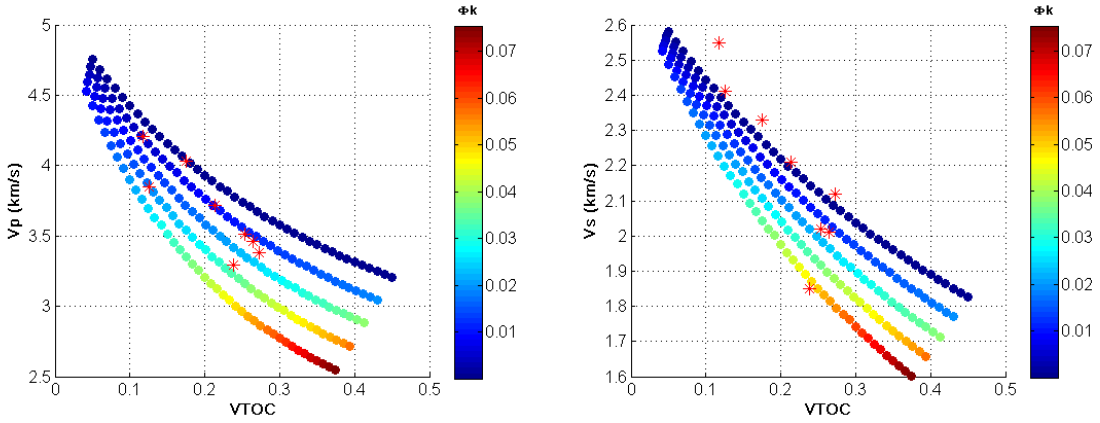

Figure 3.5.6 Left: mature organic-rich shale rock physics model: P-wave velocity (Vp) vs. kerogen volume fraction (VTOC). Right: mature organic-rich shale rock physics model: S-wave velocity (Vs) vs. kerogen volume fraction (VTOC). Red stars indicate the Bakken shale data with Ro (%) from 0.6 to 1.1 from Vernik and Nur (1992).

Figure 3.5.6 shows that the modeled P- and S-wave (normal-to-bedding) velocities will decrease with increasing TOC, which follows the same trend as the immature case. The

kerogen-related porosities ϕ_k are larger than those of immature rock, so more kerogen is decomposed to form oil and gas, and kerogen-related pores contribute significantly to the total porosity. For the same kerogen volume values, more kerogen-related pores form and the rock becomes more mature. The model shows five different crack densities (ranging from 0 to 0.2, from top to bottom), with various kerogen volumes and different kerogen-related porosities. Greater kerogen volumes and kerogen-related porosities both lower the P- and S-wave velocities. Eight Bakken shale samples data with Ro (%) ranging from 0.6 to 1.1 (Vernik and Nur, 1992) are plotted and marked with red stars. As a whole, they follow the trend, and most of them fall within the range of the predicted relationship between Vp-VTOC, Vs-VTOC, bulk density-VTOC, and P-impedance-VTOC.

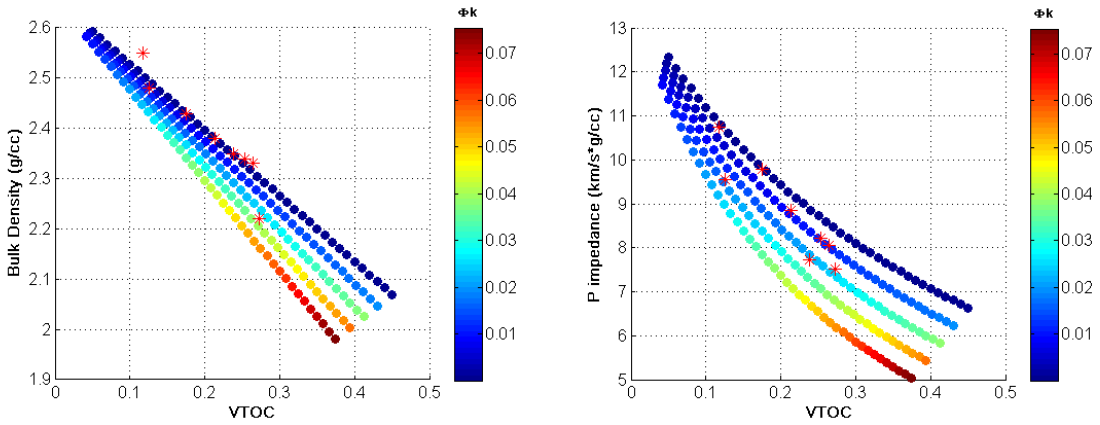

Figure 3.5.7 Left: mature organic-rich shale rock physics model: bulk density vs. kerogen volume fraction (VTOC). Right: mature organic-rich shale rock physics model: P-wave impedance vs. kerogen volume fraction (VTOC). Red stars indicate the Bakken shale data with Ro (%) from 0.6 to 1.1 from Vernik and Nur (1992).

In Figure 3.5.7, the bulk density is correlated with the kerogen volume as well as the pore space created during kerogen maturation. Five trend curves, from top to bottom, represent crack densities of 0, 0.05, 0.1, 0.15, and 0.2, respectively. The S-wave velocity, bulk

density, and Vp/Vs ratio values of the Bakken core sample with a kerogen volume of 11.8% are outside of the lower bound of the mature organic-rich shale model, which may be because less clay exists in that sample, causing higher S-wave velocity and density. In Figure 3.5.8, the Vp/Vs ratios decrease significantly with increasing maturity levels (kerogen-related pores) or kerogen volumes, which can be as low as 1.6. When the kerogen amount is lower (VTOC < 25%), an increasing amount of kerogen dominantly lowers the Vp/Vs ratio; when the amount of kerogen is higher (VTOC > 25%), the increasing level of maturity dominantly lowers the Vp/Vs ratio.

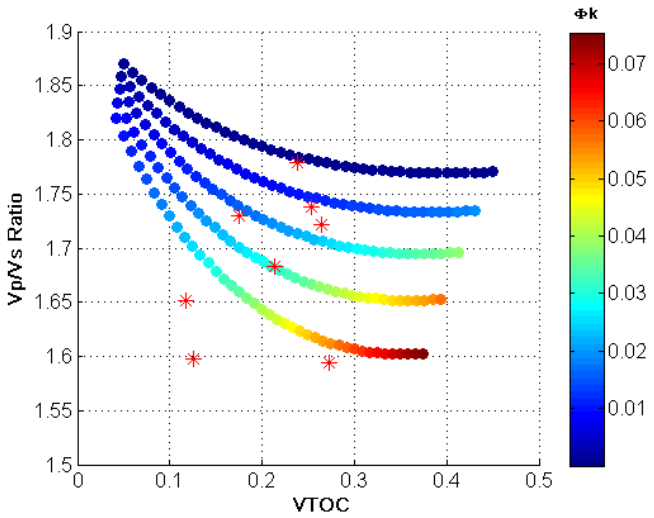

Figure 3.5.8 Mature organic-rich shale rock physics model: Vp/Vs ratio vs. kerogen volume fraction (VTOC). Red stars indicate the Bakken shale data with Ro (%) from 0.6 to 1.1 from Vernik and Nur (1992).

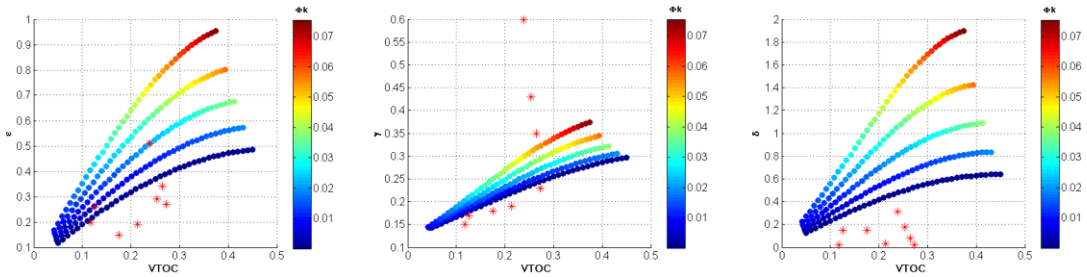

Figure 3.5.9 Thomsen's parameters varying with volumes of kerogen and kerogen-related porosities. Left: ε vs. kerogen volume fraction (VTOC). Middle: γ vs. kerogen volume fraction (VTOC). Right: δ vs. kerogen volume fraction (VTOC). Red stars indicate the Bakken shale data with Ro (%) from 0.6 to 1.1 from Vernik and Nur (1992).

Kerogen is considered as an isotropic material, but its particle alignment, which is parallel to the shale bedding, can induce strong polar anisotropy. The modeled anisotropies results in the mature rock model are stronger than the modeled results in the immature rock model, resulting from differences in properties (such as stiffness and density, etc.) between the organic part and the inorganic matrix part increasing during kerogen maturation. Organic matter becomes much softer than the rock matrix, and the anisotropy induced by bedding-aligned kerogen can increase. Figure 3.5.9 demonstrates that, with increasing organic matter or maturity level, the Thomsen's parameters increase. The reason for the overestimation of the anisotropies may be missing microstructure information about particle alignments or lower aspect ratios for some inclusions, such as clay minerals, kerogen, etc., which will increase the difference between the stiffness constant along and normal to the bedding.

Overmature model

In overmature shale reservoirs, active kerogen is completely cracked to form oil and gas, organic matter becomes denser and stiffer (Prasad, 2011; Alfred and Vernik, 2012). The solid material remains in the original space of the kerogen, including the maturation reaction residue and graphite (Figure 3.3.3 (right) and Figure 3.3.4 (right)). We can assume that the residue has the same elastic properties as the kerogen but a different reactant active energy. A bulk modulus of 7.98 GPa and a shear modulus of 4.18 GPa are applied, which was used by Lucier *et al.* (2011) when they dealt with the Haynesville gas shale with a vitrinite reflectance Ro (%) ranging from 2.0 to 2.8. A density of 1.4 g/cc is applied. According to the organic-rich shale basin model built in the last section, we can take type II kerogen as an example (Figure 3.3.3 (right)); the gas mass concentration is about 50%, and the remaining solid consists of volume fractions of approximately 75% residue and 25% graphite. Therefore, the elastic properties of the solid material in the organic phase can be modeled using the self-consistent approximations (SCA), since kerogen and graphite particles are sheet-like shapes, and we can use proper aspect ratios to simulate their geometries numerically. As the rock is overcooked, all of the oil cracks to form gas and the water evaporates; thus, the pore fluid in kerogen-related pores and the mineral matrix pores consists only of gas. The crack densities are higher than those of the mature case, which simulates more organic matter decomposition. However, the maturation-generated pore spaces may connect and be squeezed into low aspect ratio pores due to higher overburden stress at greater depth. The inorganic matrix in our model consists of a mineral combination of 20% quartz, 60% calcite, and 20% clay. The matrix

porosity is 1%, and the kerogen-related porosities can reach 5%, as shown in the colored bars in Figures 3.5.10 to 3.5.13. Other parameters used in the overmature model are listed in Table 3.5.3. Figures 3.5.10 to 3.5.13 demonstrate the modeled rock properties with different kerogen volume fractions (VTOC) and kerogen-related porosities (maturity level). Three curves from the top to the right in Figures 3.5.10, 3.5.11, and 3.5.12 indicate constant crack densities of 0.3, 0.4, and 0.5, respectively.

Table 3.5.3 Parameters used in the overmature organic-rich shale model.

Matrix porosity (ϕ_{nk})	1%	**$K_{graphite}$**	4.79 GPa
Matrix-related pore aspect ratio (α_{nk})	0.1	**$\mu_{graphite}$**	4.54 GPa
Kerogen-related porosity (ϕ_k)	0.5-4.5%	**$\rho_{graphite}$**	1.9 g/cc
Kerogen-related pore aspect ratio (α_k)	0.05	**$K_{kerogen}$**	7.98 GPa
Kerogen mineral aspect ratio ($\alpha_{kerogen}$)	0.1	**$\mu_{kerogen}$**	4.18 GPa
Clay mineral aspect ratio (α_{clay})	0.1	**$\rho_{kerogen}$**	1.4 g/cc
Graphite crystal aspect ratio ($\alpha_{graphite}$)	0.1	**K_{gas}**	0.07 GPa
Crack density (ε)	0.3-0.5	**μ_{gas}**	0 GPa
Initial amount of kerogen volume fraction	5%-45%	**ρ_{gas}**	0.1 g/cc

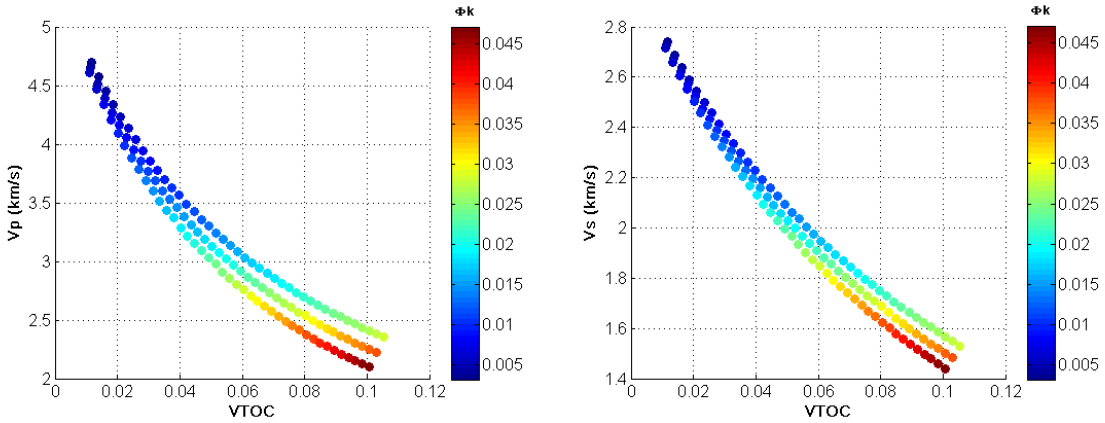

Figure 3.5.10 Left: mature organic-rich shale rock physics model: P-wave velocity (Vp) vs. kerogen volume fraction (VTOC). Right: mature organic-rich shale rock physics model: S-wave velocity (Vs) vs. kerogen volume fraction (VTOC).

Figure 3.5.10 shows the modeled P- and S-wave (normal-to-bedding) velocities. Both of them decrease with increasing kerogen, which follows the same trend as the immature and mature cases. The model shows us three different crack densities (0.3 in the top curve, 0.4 in the middle curve, and 0.5 in the bottom curve) with various kerogen volumes and different kerogen-related porosities. The kerogen-related porosities ϕ_k are larger than those of immature rock (< 0.5%) but smaller than those of mature rock (~8%). This is because the much lower aspect ratio of kerogen-related pores is applied, and it creates fewer kerogen-related pores, even if the crack density is higher than that of the mature case (equation 4.4.14). For the same kerogen volume values, the more kerogen-related pores are formed and the more mature the rock becomes, which softens the rock for P- and shear velocities. Increased kerogen volumes and kerogen-related porosities both lower P- and S-wave velocities.

Figure 3.5.11 shows the relationships between the bulk density or P-impedance and kerogen volumes; they are color-coded with kerogen-related porosities (maturity level). Rock porosities are correlated with kerogen volumes.

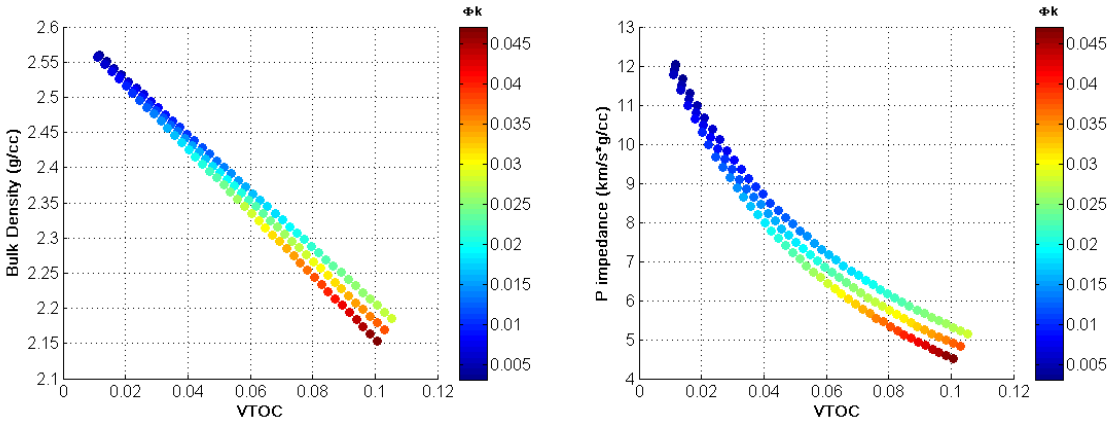

Figure 3.5.11 Left: immature organic-rich shale rock physics model: bulk density vs. kerogen volume fraction (VTOC). Right: immature organic-rich shale rock physics model: P- wave impedance vs. kerogen volume fraction (VTOC).

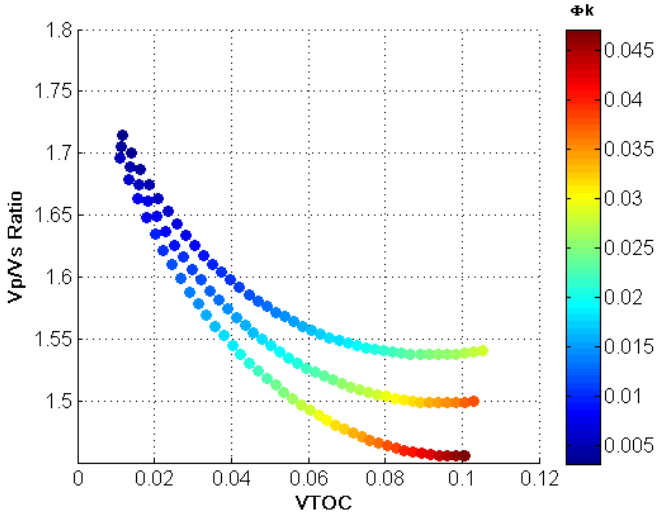

Figure 3.5.12 Immature organic-rich shale rock physics model: Vp/Vs ratio vs. kerogen volume fraction (VTOC).

In Figure 3.5.12, the Vp/Vs ratio decreases significantly with increasing VTOC, especially for the organic part with higher crack density (0.5), which can be as low as 1.45. When the kerogen amount is less (VTOC < 25%), an increasing amount of kerogen dominantly lowers the Vp/Vs ratio; when the kerogen amount is higher (VTOC < 25%), the increasing level of maturity (crack density or corresponding kerogen-related porosity) dominantly lowers the Vp/Vs ratio.

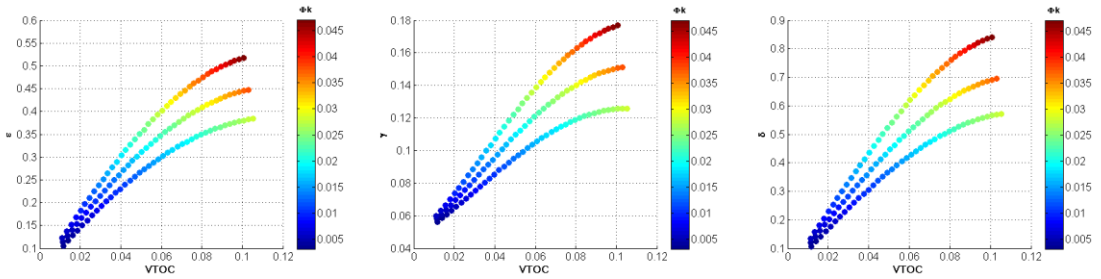

Figure 3.5.13 Thomsen's parameters varying with volumes of kerogen and kerogen-related porosities. Left: ε vs. kerogen volume fraction (VTOC). Middle: γ vs. kerogen volume fraction (VTOC). Right: δ vs. kerogen volume fraction (VTOC).

Kerogen and graphite are considered as isotropic materials, but their mixture alignments along shale bedding can induce stronger polar anisotropy. When gas-filled kerogen-related pores of quite a low aspect ratio are added as inclusions into organic matter, the rock anisotropies increase since the properties of the effective medium of organic matter differ significantly from the properties of the rock inorganic matrix. The modeled anisotropies results are shown in Figure 3.5.13. With increasing organic matter, more kerogen particles are aligned parallel to the bedding plane, and the Thomsen's parameters (Thomsen, 1986) increase, which is in accordance with the immature and mature models'

results that an increasing amount of organic matter or an increasing maturity level (kerogen-related porosity) will raise the Thomsen's parameters.

Chapter 4 Summary

To study the mineralogical effects on Vp-Vs relations and velocity anisotropies of organic-rich shales, this thesis has analyzed Vp-Vs data measured on three types of reservoir shales: silica-rich shales (the Woodford shale), clay-rich shales (gas shale from north Texas), and calcareous shales (the Haynesville and Eagle Ford shale). Silica-rich shales generally have low Vp/Vs ratios varying from 1.5 to 1.7, clay-rich shales' Vp/Vs ratios vary from 1.5 to 1.8, and calcareous shales have Vp/Vs ratios ranging from 1.6 to 2.0. The P-wave and S-wave anisotropies show certain correlations in these three types of organic-rich shales. To interpret the data, a two-layer model was built based on the Backus average. The modeling results suggest that silica-rich shales have larger γ/ε ratios than calcareous shales and clay-rich shales, but calcareous shales have higher P-impedance than clay-rich shales. The γ/ε ratio can be used as a mineral indicator in lithology inversion. In addition, well logging data from the Barnett shale are analyzed. Silica-rich shales has low Vp/Vs ratios ranging from 1.45 to 1.55. Clay-rich shales and calcareous shales can have highest value of Vp/Vs of 1.7, but P-impedances of clay-rich and calcareous shales are lowest and highest, respectively. These observations are consistent with core analysis and model prediction.

To study the effects of organic matter on Vp-Vs relations and velocity anisotropies of organic-rich shales, organic-rich shales' evolution and organic matter maturation were

studied and modeled numerically. Unconventional reservoir basin models were built for three types of kerogen, which can provide physical constraints to model substances phases and proportions during organic matter maturation. Rock physics models using effective medium theory are proposed to describe organic-rich shales' properties at various maturity levels: immature, mature, and overmature. These models strive to follow the microstructure and physical properties of rocks. In the immature rock, total porosities are low, volumes of organic matter are high, densities are closely related to volumes of organic matter, and Vp/Vs ratios are higher than the mature and overmature shales; the mature shales have largest total porosities and intermediate Vp/Vs ratios; the overmature shales have intermediate total porosities, the least amount of organic matter and the lowest Vp/Vs ratios. The immature and mature models match well with the Bakken shale core data. The modeled results can help people understand sensitivity of Vp/Vs ratios or anisotropies on TOC or maturity levels. When TOC is high, higher crack density (maturity level) dominates decrease of Vp/Vs ratios and increase of anisotropies; when TOC is low, higher TOC dominates decrease of Vp/Vs ratios and increase of anisotropies.

REFERENCES

Abousleiman, Younane, Minh Tran, Son Hoang, Christopher Bobko, Alberto Ortega, and Franz-Joseph Ulm. "Geomechanics field and laboratory characterization of the Woodford Shale: The next gas play." SPE Annual Technical Conference and Exhibition (2007): 1-14.

Alfred, Dicman, and Lev Vernik. "A new petrophysical model for organic-rich shales." SPWLA 53rd Annual Logging Symposium (2012): 16-20.

Backus, George E. "Long-wave elastic anisotropy produced by horizontal layering." Journal of Geophysical Research 67, no. 11 (1962): 4427-4440.

Berryman, James G. "Long-wavelength propagation in composite elastic media I. Spherical inclusions." The Journal of the Acoustical Society of America 68 (1980): 1809-1831.

Berryman, James G. "Mixture theories for rock properties." In "Rock Physics & Phase Relations: A Handbook of Physical Constants," first edition, T.J. Ahrens. Washington, DC: American Geophysical Union (1995): 205-228.

Berryman, James G., Steven R. Pride, and Herbert F. Wang. "A differential scheme for elastic properties of rocks with dry or saturated cracks." Geophysical Journal International 151, no. 2 (2002): 597-611.

Biot, Maurice A. "Theory of propagation of elastic waves in a fluid-saturated porous solid. I. Low-frequency range." The Journal of the Acoustical Society of America 28 (1956): 168-191.

Budiansky, Bernard. "On the elastic moduli of some heterogeneous materials." Journal of the Mechanics and Physics of Solids 13, no. 4 (1965): 223-227.

Carcione, José M., and Anthony F. Gangi. "Gas generation and overpressure: effects on seismic attributes." Geophysics 65, no. 6 (2000): 1769-1779.

Carcione, José M., and Fabio Cavallini. "Poisson's ratio at high pore pressure." Geophysical Prospecting 50, no. 1 (2002): 97-106.

Carcione, José M., Hans B. Helle, and Per Avseth. "Source-rock seismic-velocity models: Gassmann versus Backus." Geophysics 76, no. 5 (2011): N37-N45.

Castagna, John P., Michael L. Batzle, and Raymond L. Eastwood. "Relationships between compressional-wave and shear-wave velocities in clastic silicate rocks." Geophysics 50, no. 4 (1985): 571-581.

Ciz, Radim, and Serge A. Shapiro. "Generalization of Gassmann equations for porous media saturated with a solid material." Geophysics 72, no. 6 (2007): A75-A79.

Cleary, Michael P., Shaw-Ming Lee, and I-Wei Chen. "Self-consistent techniques for heterogeneous media." Journal of the Engineering Mechanics Division 106, no. 5 (1980): 861-887.

Crain, E. R. "Crain's Petrophysical Handbook." [Online]. (2011): Available at http://www.spec2000.net/

Dræge, Anders, Morten Jakobsen, and Tor Arne Johansen. "Rock physics modelling of shale diagenesis." Petroleum Geoscience 12, no. 1 (2006): 49-57.

Gassmann, Fritz. "Elasticity of porous media." Vierteljahrschrift der Naturforschenden gesellschaft in Zurich 96 (1951): 1-21.

Guo, Zhiqi, Xiang-Yang Li, Cai Liu, Xuan Feng, and Ye Shen. "A shale rock physics model for analysis of brittleness index, mineralogy and porosity in the Barnett Shale." Journal of Geophysics and Engineering 10, no. 2 (2013): 1-11.

Han, De-Hua, Amos Nur, and Dale Morgan. "Effects of porosity and clay content on wave velocities in sandstones." Geophysics 51, no. 11 (1986): 2093-2107.

Hashin, Zvi, and S. Shtrikman. "A variational approach to the theory of the elastic behaviour of multiphase materials." Journal of the Mechanics and Physics of Solids 11, no. 2 (1963): 127-140.

Hill, Richard. "The elastic behaviour of a crystalline aggregate." Proceedings of the Physical Society. Section A 65, no. 5 (1952): 349-354.

Hill, Richard "A self-consistent mechanics of composite materials." Journal of the Mechanics and Physics of Solids 13, no. 4 (1965): 213-222.

Hornby, Brian E., Larry M. Schwartz, and John A. Hudson. "Anisotropic effective-medium modeling of the elastic properties of shales." Geophysics 59, no. 10 (1994): 1570-1583.

Jakobsen, Morten, and Tor Arne Johansen. "Anisotropic approximations for mudrocks: A seismic laboratory study." Geophysics 65, no. 6 (2000): 1711-1725.

Johnston, Joel E., and Nikolas I. Christensen. "Seismic anisotropy of shales." Journal of Geophysical Research: Solid Earth (1978–2012) 100, no. B4 (1995): 5991-6003.

Karastathis, Argyrios. "Petrophysical measurements on tight gas shale." PhD dissertation, University of Oklahoma (2007).

Kuster, Guy T., and M. Nafi Toksöz. "Velocity and attenuation of seismic waves in two-phase media: Part I. Theoretical formulations." Geophysics 39, no. 5 (1974): 587-606.

Lucier, Amie M., Ronny Hofmann, and L. Taras Bryndzia. "Evaluation of variable gas saturation on acoustic log data from the Haynesville Shale gas play, NW Louisiana, USA." The Leading Edge 30, no. 3 (2011): 300-311.

Luo, Xiaorong, and Guy Vasseur. "Geopressuring mechanism of organic matter cracking; numerical modeling." AAPG Bulletin 80, no. 6 (1996): 856-874.

Mavko, Gary, Tapan Mukerji, and Jack Dvorkin. "The Rock Physics Handbook: Tools for Seismic Analysis of Porous Media." Second edition, New York: Cambridge University Press (2009).

Mba, Kenechukwu, Manika Prasad, and Mike Batzle. "The maturity of organic-rich shales using microimpedance analysis." SPE Annual Technical Conference and Exhibition (2010).

Nishizawa, Osamu. "Seismic velocity anisotropy in a medium containing oriented cracks." Journal of Physics of the Earth 30, no. 4 (1982): 331-347.

Norris, Andrew N. "A differential scheme for the effective moduli of composites." Mechanics of materials 4, no. 1 (1985): 1-16.

Ortega, J. Alberto, Franz-Josef Ulm, and Younane Abousleiman. "The effect of the nanogranular nature of shale on their poroelastic behavior." Acta Geotechnica 2, no. 3 (2007): 155-182.

Passey, Quinn R., S. Creaney, J. B. Kulla, F. J. Moretti, and J. D. Stroud. "A practical model for organic richness from porosity and resistivity logs." AAPG Bulletin 74, no. 12 (1990): 1777-1794.

Passey, Quinn R., Kevin Bohacs, William Esch, Robert Klimentidis, and Somnath Sinha. "From oil-prone source rock to gas-producing shale reservoir-geologic and petrophysical characterization of unconventional shale gas reservoirs." International Oil and Gas Conference and Exhibition in China (2010): 1-29.

Prasad, Manika, Kenechukwu Mba, Tracy Sadler, and Mike Batzle. "Maturity and impedance analysis of organic-rich shales." SPE Reservoir Evaluation & Engineering 14, no. 5 (2011): 533-543.

Ruiz, Franklin J. "Porous grain model and equivalent elastic medium approach for predicting effective elastic properties of sedimentary rocks." PhD dissertation, Stanford University (2009).

Ruiz, Franklin, and Ilgar Azizov. "Tight shale elastic properties using the soft-porosity and single aspect ratio models." 2011 SEG Annual Meeting (2011a).

Ruiz, Franklin, and Ilgar Azizov. "Fluid substitution in tight shale using the soft-porosity model." 2011 SEG Annual Meeting (2011b).

Sarout, Joël, and Yves Guéguen. "Anisotropy of elastic wave velocities in deformed shales: Part 1—Experimental results." Geophysics 73, no. 5 (2008): D75-D89.

Sayers, Colin M. "The effect of anisotropy on the Young's moduli and Poisson's ratios of shales." Geophysical Prospecting 61, no. 2 (2013): 416-426.

Seewald, Jeffrey S. "Organic–inorganic interactions in petroleum-producing sedimentary basins." Nature 426, no. 6964 (2003): 327-333.

Shuey, Ralph T. "A simplification of the Zoeppritz equations." Geophysics 50, no. 4 (1985): 609-614.

Sondergeld, Carl H., and Chandra S. Rai. "Elastic anisotropy of shales." The Leading Edge 30, no. 3 (2011): 324-331.

Thomsen, Leon. "Weak elastic anisotropy." Geophysics 51, no. 10 (1986): 1954-1966.

Thomsen, Leon. "Understanding Seismic Anisotropy in Exploration and Exploitation." No. 5. SEG Books, (2002).

Tosaya, Carol Ann. "Acoustical Properties of Clay-bearing Rocks." PhD dissertation, Stanford University (1982).

Ulm, Franz-Josef, and Younane Abousleiman. "The nanogranular nature of shale." Acta Geotechnica 1, no. 2 (2006): 77-88.

Vanorio, Tiziana, Tapan Mukerji, and Gary Mavko. "Elastic anisotropy, maturity, and maceral microstructure in organic-rich shales." 2008 SEG Annual Meeting (2008): 1635-1639.

Vernik, Lev. "Hydrocarbon-generation-induced microcracking of source rocks." Geophysics 59, no. 4 (1994): 555-563.

Vernik, Lev, and Xingzhou Liu. "Velocity anisotropy in shales: A petrophysical study." Geophysics 62, no. 2 (1997): 521-532.

Vernik, Lev, and Amos Nur. "Ultrasonic velocity and anisotropy of hydrocarbon source rocks." Geophysics 57, no. 5 (1992): 727-735.

Vernik, Lev, and Jadranka Milovac. "Rock physics of organic-rich shales." The Leading Edge 30, no. 3 (2011): 318-323.

Wood, Albert B. "A Textbook of Sound: the Physics of Vibrations." Bell and Sons (1955).

Wu, Tai Te. "The effect of inclusion shape on the elastic moduli of a two-phase material." International Journal of Solids and Structures 2, no. 1 (1966): 1-8.

Yan, Fuyong, and De-Hua Han, "Measurement of elastic properties of kerogen." Fluid/DHI consortium annual report (2012): 1-7.

Yan, Fuyong, and De-Hua Han. "Physical constraints on c_{13} and Thomsen parameter delta for VTI rocks." 2013 SEG Annual Meeting (2013): 1-5.

Zhu, Yaping, Enru Liu, Alex Martinez, Michael A. Payne, and Christopher E. Harris. "Understanding geophysical responses of shale-gas plays." The Leading Edge 30, no. 3 (2011): 332-338.

Zhu, Yaping, Shiyu Xu, Michael Payne, Alex Martinez, Enru Liu, Chris Harris, and Kaushik Bandyopadhyay. "Improved rock-physics model for shale gas reservoirs." 2012 SEG Annual Meeting (2012): 1-5.

Zimmerman, Robert W. "Elastic moduli of a solid containing spherical inclusions." Mechanics of Materials 12, no. 1 (1991): 17-24.